



UNIVERSITÉ DE FRIBOURG SUISSE
UNIVERSITÄT FREIBURG SCHWEIZ

Département de Physique
Université de Fribourg (Suisse)

**X-ray resonant Raman scattering
in light elements
and
Relative detection efficiency
of Charge Coupled Devices**

THÈSE

Présentée à la Faculté des Sciences de l'Université de Fribourg (Suisse)
pour l'obtention du grade de
Doctor rerum naturalium

Jakub Szlachetko
Pologne

Numéro de la thèse: 1568

Saint-Paul
(2007)

Acceptée par la Faculté des Sciences de l'Université de Fribourg (Suisse)
sur la proposition de:

Prof. Dr. Antoine Weis, Université de Fribourg (Président de Jury)

Prof. Dr. Jean-Claude Dousse, Université de Fribourg (Directeur de thèse)

Prof. Dr. Marek Pajek, Swietokrzyska Academy, Pologne (Corapporteur)

Dr. Joanna Hoszowska, Université de Fribourg (Corapporteure)

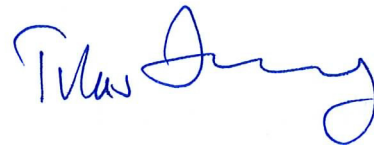
Fribourg, 27 Juin 2007

Le Directeur de thèse



Prof. Dr. Jean-Claude Dousse

Le Doyen



Prof. Dr. Titus Jenny

*”Nauka jest jak niezmierne morze
Im więcej jej pijesz, tym bardziej jesteś spragniony”
Stefan Żeromski*

Contents

Résumé	7
Abstract	11
Part I:	
Relative detection efficiency of back- and front-illuminated CCD cameras for x-rays between 1 keV and 18 keV	17
Part II:	
High-resolution study of x-ray resonant Raman scattering at the K-edge of silicon	47
High-resolution study of the x-ray resonant Raman scattering process around the 1s absorption edge for aluminium, silicon and their oxides	57
List of publications	83
Curriculum vitae	87
Acknowledgments	89

Résumé

Cette thèse de doctorat comprend deux projets de recherche qui se rattachent au domaine de la physique atomique, plus précisément à celui des couches atomiques internes. Le premier projet est consacré à une étude des efficacités relatives pour la détection de rayons X de deux caméras CCD de type différent, l'une de type "front-illuminated", l'autre de type "back-illuminated". Le second projet concerne la diffusion Raman résonnante de rayons X. Cette étude est elle-même subdivisée en deux parties, la première concernant la diffusion Raman sur un échantillon de silicium, la seconde reprenant des résultats de la première étude d'une façon plus approfondie et l'étendant à d'autres échantillons (Al, Al₂O₃, SiO₂).

Efficacité relative de caméras CCD de type "back-illuminated" et "front-illuminated" pour la détection de rayons X entre 1 keV et 18 keV

Les détecteurs CCD sont utilisés dans un grand nombre de domaines scientifiques différents, en particulier dans celui de la spectroscopie X de haute résolution. Cependant, pour une analyse détaillée des données acquises avec de tels détecteurs, leur réponse spectrale doit être connue de façon précise. En vue de choisir le détecteur le plus judicieux pour le projet de diffusion Raman, les performances de CCD "back-illuminated" et "front-illuminated" ont été déterminées et comparées pour une série de rayons X caractéristiques d'énergie comprise entre 1 keV et 18 keV. Les mesures ont été réalisées à Fribourg au moyen d'un spectromètre à cristal incurvé de type von Hamos, utilisant le premier CCD, puis le second, pour la détection des rayons X diffractés. A partir de ces mesures, l'efficacité de transfert de charges, la linéarité de la réponse en énergie, le niveau du bruit et l'efficacité quantique des deux détecteurs ont été déterminés.

Il a été trouvé que les performances du CCD "front-illuminated" étaient amoindries par un problème lié au transfert de charge alors que la caméra "back-illuminated" souffrait, elle, d'un effet de partage des charges entre plusieurs pixels, cet effet de "charge splitting" touchant aussi l'autre détecteur mais de façon moindre et surtout pour des photons de plus haute énergie. Pour résoudre ces problèmes des logiciels de correction d'images ont été développés, lesquels ont permis d'améliorer considérablement l'efficacité quantique des deux détecteurs.

La dépendance en énergie du "splitting effect" a été étudiée pour les deux caméras. Les différences ont pu être expliquées par des simulations de Monte-Carlo. Il a été démontré en particulier que cet effet avait lieu dans la partie "field free" du CCD, laquelle est située du côté de la face irradiée pour le CCD "back-illuminated" et à l'opposé pour le CCD "front-illuminated". Ceci a permis de comprendre pourquoi cet effet ne varie pas de la même manière avec l'énergie des photons pour les deux détecteurs.

A partir de l'intensité des raies de fluorescence mesurées, le rapport d'efficacité quantique des deux CCD a pu être obtenu en fonction de l'énergie des rayons X incidents. Les résultats ont montré que la caméra "back-illuminated" est plus efficace jusqu'à environ 4.5 keV alors qu'au-dessus de cette énergie, la caméra "front-illuminated" est supérieure, un rapport d'efficacité quantique d'environ 2.5 étant observé aux énergies les plus hautes. Les résultats obtenus dans

cette première étude ont revêtu une importance particulière pour la réalisation du projet de diffusion Raman, indiquant que pour les énergies inférieures à 2 keV correspondant aux photons Raman de l'Al et du Si, la caméra "back-illuminated" était clairement la plus appropriée.

Les résultats de cette étude ont été soumis récemment pour publication dans le journal *Review of Scientific Instruments*.

Diffusion Raman résonnante de rayons X pour l'aluminium, le silicium et leur oxyde

La diffusion Raman résonnante est un processus de 2^{ème} ordre dans lequel un photon incident est absorbé par l'atome puis réémis par ce dernier. Plus précisément, un électron du cœur de l'atome est photo-excité dans un état lié juste au-dessus du niveau de Fermi. L'état intermédiaire virtuel se désexcite quasi-instantanément, la lacune de cœur étant comblée par un électron provenant d'une autre couche profonde plus extérieure. Cette transition électronique est accompagnée de l'émission simultanée d'un photon. La diffusion de Raman est peu probable sauf si le photon incident possède une énergie inférieure mais très proche de l'un des bords d'absorption de l'échantillon irradié. Dans ce cas, le processus devient un phénomène de résonance et sa probabilité augmente de plusieurs ordres de grandeur. La diffusion Raman résonnante de rayons X (XRRS en abrégé) représente une méthode efficace pour étudier la structure électronique des solides. De ce point de vue, la méthode XRRS est complémentaire aux techniques basées sur l'absorption de rayons X.

Dans le cas particulier du silicium, l'étude expérimentale du processus XRRS présente un intérêt supplémentaire important. La fabrication de monocristaux de Si de plus en plus purs est l'une des priorités de l'industrie des semi-conducteurs. Le problème est qu'à l'heure actuelle les cristaux produits ont une pureté telle qu'il devient très difficile de déterminer cette dernière. La méthode la plus performante pour la détermination du pourcentage d'éléments-traces dans des "wafers" de silicium ultra-purs est la méthode TXRF (Total reflection X-Ray Fluorescence) combinée avec des faisceaux monochromatiques de rayonnement synchrotronique. Plusieurs expériences ont cependant montré que dans cette méthode, le seuil de détectabilité des impuretés d'éléments légers est limité par la diffusion Raman résonnante. Dans la méthode TXRF appliquée au silicium, l'énergie des photons incidents est en effet choisie en dessous du bord d'absorption 1s du silicium pour éviter la production des raies de fluorescence K de ce dernier, lesquelles masqueraient complètement les signaux de fluorescence beaucoup plus faibles des impuretés. L'énergie des photons incidents est cependant choisie juste au-dessous du bord K du Si, ceci afin de pouvoir exciter la fluorescence K des impuretés d'éléments légers voisins comme par exemple l'aluminium. Pour cette raison, les conditions de résonance pour la diffusion Raman sont remplies et les faibles raies de fluorescence des atomes légers constituant les impuretés sont alors masquées par le spectre continu de rayons X de la diffusion Raman. Jusqu'à présent, l'intensité du spectre Raman parasite était estimée à partir de modèles théoriques car il n'existait aucune mesure de haute résolution du processus XRRS.

Les mesures ont été réalisées à la source de rayonnement synchrotronique européenne (ESRF), à Grenoble. Les spectres Raman ont été mesurés en haute résolution au moyen du spectromètre

à cristal von Hamos de Fribourg, lequel a été installé sur la ligne de faisceau ID-21. Comme indiqué précédemment, pour la détection des photons diffractés par le cristal du spectromètre, la caméra de type "back-illuminated" a été utilisée. Les spectres Raman d'échantillons solides de Al, Al₂O₃, Si et SiO₂ ont été mesurés pour des faisceaux de photons incidents de différentes énergies choisies en dessous des bords d'absorption K de l'aluminium et du silicium.

Comme prédit par la théorie, les spectres Raman mesurés sont caractérisés par un point-limite (cut-off) correspondant à l'énergie maximale du spectre Raman et d'une longue queue à basse énergie s'étalant théoriquement jusqu'à l'énergie zéro. Pour les spectres mesurés avec des énergies de faisceau différentes, ces queues de basse énergie se superposent et tendent à se confondre, en accord avec les prédictions théoriques. L'analyse des données a montré que la forme des spectres mesurés était bien reproduite par des calculs basés sur le modèle de Kramers-Heisenberg, à condition d'utiliser dans ces calculs des distributions réalistes pour les forces d'oscillateur. Ces distributions ont pu être déduites des spectres Raman expérimentaux pour les quatre cibles mesurées. Les distributions de force d'oscillateur obtenues présentent des structures tout à fait semblables à celles trouvées dans des mesures d'absorption. En fait, ce projet représente la première vérification expérimentale de prédictions théoriques concernant la présence de structures similaires dans les spectres d'absorption et d'émission de rayons X.

Les sections efficaces totales pour le processus XRRS ont été déterminées en fonction de l'énergie des photons incidents. La dépendance en énergie des sections efficaces a pu être bien reproduite par la théorie. Pour le silicium, les sections efficaces ont été comparées aux quelques résultats expérimentaux existants. Un bon accord a été trouvé. Pour ce même élément, en variant l'énergie du faisceau de rayonnement synchrotronique à travers le bord d'absorption K, la photo-excitation 1s-3p a pu être observée expérimentalement pour la première fois. Il a été trouvé que l'évolution de la section efficace de cette excitation discrète en fonction de l'énergie du faisceau était bien reproduite par des calculs DOS concernant la densité de probabilité des états inoccupés 3p du Si.

Cette deuxième partie de la thèse a fait l'objet de deux publications, l'une dans Physical Review Letters 97, 073001 (2006), l'autre dans Physical Review A 75, 022512 (2007).

Abstract

The present Ph.D. thesis includes two research projects related to the field of Inner-Shell Atomic Physics. The first project is devoted to the relative x-ray detection efficiency of front- and back-illuminated Charge Coupled Devices. The second one concerns the study of the x-ray resonant Raman scattering process in silicon, aluminium and their oxides and is divided into two parts. The first part, describes the particular case of the x-ray resonant Raman process in silicon, whereas in the second one the results and the detailed analysis of the x-ray resonant spectra for aluminium, silicon, aluminum oxide and silicon dioxide are presented.

Relative detection efficiency of back- and front-illuminated CCD cameras for x-rays between 1 keV and 18 keV

The Charge Coupled Device (CCD) is a widely used detector in a variety of scientific areas including high-resolution x-ray emission spectroscopy. However, in order to obtain meaningful data an accurate spectral CCD response is required. In this project, in view of the investigation of the x-ray resonant Raman process in low-Z elements, the performances and capabilities of the front- and back-illuminated scientific grade CCD cameras were examined by measuring a variety of characteristic emission lines in the x-ray energy range from 1 keV to 18 keV. The measurements were performed by means of the high-resolution von Hamos type bent crystal spectrometer of Fribourg which was equipped with either a front-illuminated or a back-illuminated camera. The x-ray photons were monochromatized by x-ray crystal diffraction. From these measurements the charge transfer efficiency, the linearity of the energy response, the noise level and the quantum efficiency of the two CCDs were determined.

It was found that the performance of the front-illuminated camera was affected principally by poor charge transfer efficiency, whereas the back-illuminated one by a strong charge splitting effect. To circumvent these problems, dedicated software for off-line corrections of the CCD images was developed. As a consequence, a significant improvement in the detection efficiency of both CCDs was achieved.

The photon energy dependence of the charge splitting effect was determined for both cameras. The observed differences between the number of split pixel events in the back-illuminated camera and the front-illuminated one were explained with the aid of Monte Carlo simulations of photon absorption in silicon. It was confirmed that the split pixel events are created mainly in the field-free region of the CCD chip. This weak electric field layer is located at the back surface of a CCD device. As the incident photons enter the CCD from the back surface for the back-illuminated camera, whereas for the front-illuminated one from the front side, the degree of charge splitting and its photon energy dependence differs for the two cameras.

From the measured intensities of the x-ray fluorescence lines the quantum efficiency ratio of the front- to back-illuminated cameras was obtained as a function of the incident x-ray energy. The results have shown that in the x-ray energy range between 1 keV and 4.5 keV the detection efficiency of the back-illuminated CCD is much higher than that of the front-illuminated one.

For photon energies above 4.5 keV the front-illuminated camera is more efficient and at the highest measured energy a quantum efficiency ratio of 2.5 was obtained. These results were of prime importance for choosing the most efficient CCD detector for the project concerning the x-ray resonant Raman scattering in low-Z elements.

This work was submitted recently for publication to Review of Scientific Instruments.

X-ray resonant Raman scattering process in aluminium, silicon and their oxides

The x-ray Raman scattering is a photon-in and photon-out second-order process. In this process a core electron is excited into a bound state just above the Fermi level by absorption of a photon. The intermediate "virtual" state then decays radiatively, the initial core hole being filled by another inner-shell electron with simultaneous emission of a photon. Due to its resonant character, the x-ray RRS is a powerful method to study the electronic structure of solids, being complementary to the x-ray absorption techniques based on the first-order process.

In the particular case of silicon, it has been realized that the x-ray RRS process sets the limits for application of the total reflection x-ray fluorescence (TXRF) method for measuring very low concentrations of light element impurities on the surface of Si wafers. The production of ultra-clean silicon wafers is one of the most important issues for Si-based microelectronic technology. Contamination control has always been very crucial for integrated circuit manufacturing where in order to obtain high yields and maximum device performance clean wafer surfaces are critical. Several experiments have shown that the detection limit of Al impurities on the Si surface is limited by the presence of RRS x-rays. It has been shown that for incident photon energies tuned below the Si K-absorption edge in order to avoid the intense Si K fluorescence x-ray line, the RRS structure of Si is indeed overlapping with the Al K x-ray fluorescence peak. Since the TXRF technique combined with intense synchrotron x-ray sources offers new possibilities for detection of light elements in ultra-clean silicon, a precise knowledge of the x-ray Raman scattering in silicon is therefore crucial for applications of the TXRF technique in the semiconductor technology.

The experiment was performed at the European Synchrotron Radiation Facility, in Grenoble, France. The x-ray RRS spectra were measured by means of high-resolution, using the Bragg type von Hamos bent crystal spectrometer installed at the beam line ID21. For detection of x-rays in the energy range between 1.4 keV and 1.8 keV the spectrometer was equipped with the back-illuminated CCD camera. The x-ray RRS spectra were recorded for several beam energies tuned below the K-absorption edge of the measured element.

As predicted by theory the observed x-ray RRS spectra are characterized by high energy cut-offs and long low-energy tails. These tails merge together in the low energy range, no matter which beam energy is used. The data analysis has shown that the observed shapes of the x-ray RRS spectra could be well reproduced by calculations based on the Kramers-Heisenberg formalism, but only when realistic oscillator strength distributions were employed. The latter could be extracted from the acquired x-ray RRS spectra for all measured samples, namely Si, Al, Al₂O₃ and SiO₂. The so-obtained oscillator strength distributions were found to exhibit

structures similar to those observed in absorption measurements. In fact, this was a first experimental confirmation of theoretical predictions concerning the absorption-like structures in the continuum part of the x-ray RRS spectra.

The total cross sections for the x-ray RRS process were determined as a function of the beam energy. The variation of the cross sections with the beam energy could be well reproduced by theory. For Si, the cross sections were compared to the few existing experimental and theoretical data. A quite satisfactory agreement was observed. By tuning the beam energy across the 1s absorption edge of silicon, we were able to observe the discrete 1s–3p excitation for the first time. The evolution of the excitation cross section with the beam energy was found to well reproduce the probability density of unoccupied 3p states predicted by DOS calculations.

This work was published in *Physical Review Letters* 97, 073001 (2006) and in *Physical Review A* 75, 022512 (2007).

Part I

Relative detection efficiency of back- and front-illuminated CCD cameras for x-rays between 1 keV and 18 keV.

J. Szlachetko, J.-Cl. Dousse, J. Hoszowska, W. Cao, M. Szlachetko
Department of Physics, University of Fribourg, CH-1700 Fribourg, Switzerland

M. Kavcic
J. Stefan Institute, SI-1001 Ljubljana, Slovenia

High-resolution x-ray measurements were performed with a von Hamos-type bent crystal spectrometer using for the detection of the diffracted photons either a back-illuminated charge-coupled device (CCD) camera or a front-illuminated one. For each CCD the main x-ray emission lines (e.g., $K\alpha$, $K\beta$, $L\alpha$ and $L\beta$) of a variety of elements were measured in order to probe the performances of the two detectors between 1 keV and 18 keV. From the observed x-ray lines the linearity of the energy response, the noise level and the quantum efficiency ratio of the two CCD were determined.

PACS number(s): 07.77.Gx, 07.85.Fv

I. INTRODUCTION

Since the 1970s, when the charge-coupled device (CCD) was invented at the Bell Telephone Laboratories [1, 2], the CCD has become a very efficient detector used in a variety of scientific areas ([3] and references therein). The CCD, which was originally developed as a memory device, presents indeed important advantages for x-ray detection: it provides high spatial and good energy resolution, has a relatively large detection area and is characterized by an ultra low noise and a broad spectral response. In the last decades CCD

detectors have been employed in an increasing way to supplant photographic films in astronomy and imaging as well as proportional counters and semiconductor detectors in x-ray spectroscopy (see e.g. [4–7]).

Nowadays a variety of commercial CCD systems are available, with different design architecture, size and characteristics [8–11]. In general, CCD detectors can be divided up into two different types, namely back- and front-illuminated devices. In this paper we report on results of extensive characterization measurements performed with a back-illuminated CCD and a front-illuminated

one, both of scientific grade. The principal aim of the measurements was to probe and to compare the performances of the two detectors in the x-ray energy range between 1 keV and 18 keV. By measuring a variety of characteristic x-ray emission lines with a curved crystal spectrometer using the CCD devices for the detection of the diffracted x-rays, we were able to determine the quantum efficiency ratio of the two cameras as a function of the x-ray energy as well as several characteristic parameters of the detectors such as the trailing and splitting effects, the linearity of the energy response and the noise level.

II. FUNDAMENTAL CONCEPTS OF CCDS

A. Work principles

The fundamental part of the CCD detector is the Metal-Oxide Semiconductor (MOS) structure, called buried channel capacitor. A schematic transverse section through the thickness of a buried channel capacitor is shown in Fig.1a. A typical MOS capacitor consists of a p-type silicon substrate and a n-type silicon layer with a thickness of about $1 \mu\text{m}$. On the surface of the n-type side of the junction a thin, usually less than $0.1 \mu\text{m}$, silicon dioxide layer is deposited. To complete the capacitor, a metal or polysilicon gate is diffused on the

oxide surface. Any voltage applied to the gate generates an electrostatic field across the capacitor. The corresponding electrostatic potential is shown schematically in Fig.1a (blue line). Depending on the strength of the electrostatic field, two characteristic regions can be distinguished in the channel capacitor. The first one, the depletion region, which has a thickness of several microns, corresponds to the region where the potential has a sizeable value. The second one, called the field free material region is located after the depletion region at distances of $\geq \sim 10 \mu\text{m}$ from the gate. In this region the electrostatic field is nearly vanishing. As schematically shown, the electrons released in the depletion region by an ionising radiation follow the variation of the electrostatic field until they reach the lowest possible potential energy. In other words, the MOS channel capacitor can be used to create a potential energy well in which electrons can be trapped.

A second type of MOS capacitor, named surface channel capacitor, has been developed which has no n-type silicon layer. In this case the potential well is located directly on the Si-SiO₂ interface. Due to that a fraction of the electrons confined in the potential well may be trapped at the silicon-oxide interface. This causes relatively big losses in the charge transfer and therefore surface channel capacitors are not commonly used in

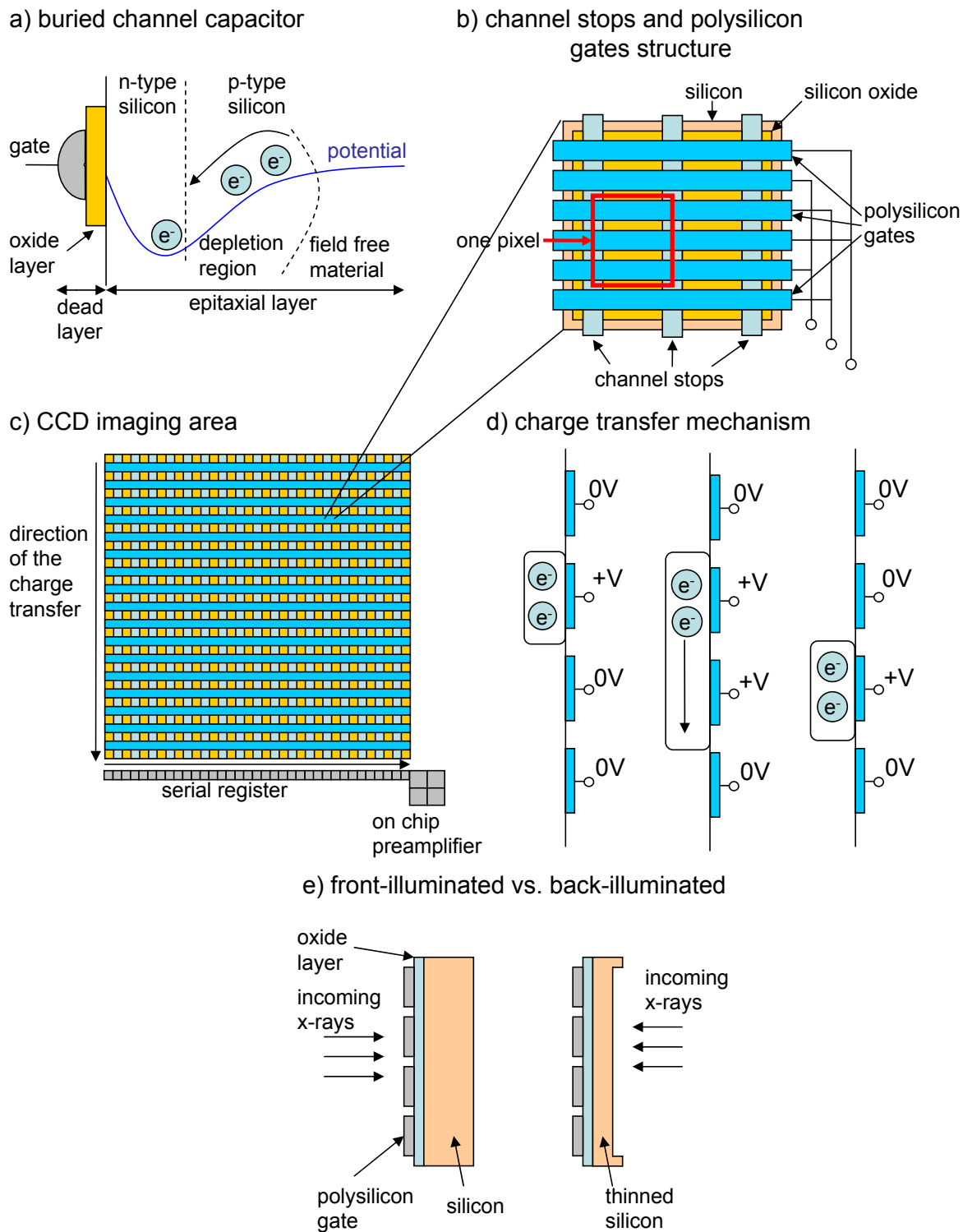


FIG. 1: Schematic drawing of a) buried channel capacitor, b) channel stops and gate structure, c) CCD imaging area and d) charge transfer mechanism. In e) the main differences between the design of front and back illuminated CCDs are shown.

the design of CCD detectors.

In order to avoid a spreading of the charges, the channel capacitor is completed with so-called channel stops (see Fig.1b) which are made of heavily doped p-type silicon. In addition polysilicon gates are implemented in the perpendicular direction to the channel stop structure. Two adjacent channel stops and three adjacent gates define the smallest area in which a charge can be localized. This small cell is called a pixel (from *Picture Element*). X-ray CCD cameras with pixel sizes of $20 \times 20 \mu m^2$ or even smaller are now easily available. If for a given pixel the potential applied to the top and bottom gates is smaller than the one applied to the middle gate, the charge can be indeed confined in the area situated beneath the middle gate, between the two channel stops, i.e., within the corresponding pixel. This three-gate architecture used in modern CCD detectors permits an easy transfer of the pixel charge by changing the voltage on the gate electrodes as shown in Fig.1d. An array of pixels forms the imaging area of the CCD which can comprise several hundreds of columns and rows of pixels [8–11]. Readout of the CCD is carried out by shifting simultaneously the pixel charges by one row or one column. For example, in the case of the vertical readout depicted in Fig.1c, the pixel charges of each row

are transferred to the next row below, the charges of the last row being transferred to the serial register. After each one-step row transfer, the pixel charges corresponding to the last transfer into the serial register are read by moving horizontally the charges pixel by pixel. Because the electric potentials resulting from the charges corresponding to the trapped electrons are extremely small (some μV), the tiny signals must be amplified before transportation to avoid any increase in the noise. This is realized by locating the preamplifier as close as possible to the CCD chip. The total time needed for the readout of a full CCD image is of the order of 0.1 sec. to 10 sec., depending on the clock rate and the size of the CCD chip. For example, the readout time of an image consisting of 1340×400 pixels is 0.54 sec. if the camera is operated at a rate of 1 MHz. Finally, the signals after further amplification are converted to digital numbers by dedicated ADCs, which permits to reconstruct the two-dimension image corresponding to the CCD charge pattern.

As mentioned above, front- and back-illuminated CCD detectors are available (Fig.1e). In the case of the front-illuminated camera, the incoming x-rays must first cross the dead layer corresponding to the polysilicon gate plus oxide layer before reaching the epitaxial layer of the CCD. Due to the

absorption of the incoming radiation in the dead layer, the detection efficiency is somewhat diminished, depending on the energy of the x-rays. As this absorption decreases with the energy of the incoming x-rays, the efficiency of front-illuminated CCDs is first growing with increasing energies, but only as long as the incident photons can be fully absorbed in the depletion region. For higher energies the efficiency decreases. In addition, for x-ray energies tuned across the K-edge of silicon there is an abrupt drop of the efficiency due to the sudden increase of the absorption coefficient of silicon at the K-edge, which results in a stronger attenuation of the incoming photons in the dead layer. For instance, as reported in [12], the detection efficiency can drop down from about 80% for x-ray energies just below the edge to 25% for photon energies just above it but in general the strength of this drop effect depends of course on the thickness and structure of the dead layer.

For back-illuminated CCDs the incoming x-rays are entering the CCD directly from the side of the epitaxial layer. Therefore the detection efficiency is improved in comparison with the front-illuminated camera, especially in the energy range for which the absorption coefficient in Si is large. In general, the efficiency drop around the 1s absorption edge of silicon is also observed

as a result of the unavoidable oxidization of the surface of the epitaxial layer but the drop is much less pronounced than that of front-illuminated CCDs. On the other hand, to avoid a too big absorption of photons in the field free material region, the silicon wafer is chemically thinned, which limits the depletion depths of back-illuminated CCDs to 10–20 μm . For this reason their efficiency is smaller than the one of front-illuminated CCDs for x-ray energies above about 4 keV.

B. CCD characterization parameters

In the following, a brief description of the main parameters used in the characterization of CCDs is given.

1. Charge collection efficiency (CCE)

The charge collection efficiency describes the capability of the channel capacitor to collect charges. The CCE depends in particular on the full well capacity, which gives the maximum number of electrons that can be trapped within a single pixel.

2. Charge transfer efficiency (CTE)

The charge which is collected in a single pixel must be transported through the CCD array to the serial register and then to the

preamplifier. During this transfer some fraction of the charge might get lost due to the mechanism of the charge transfer or the "design trap" effect reported in [3]. The charge transfer efficiency is expressed as the ratio of the charge transferred from a pixel to the next one. For scientific grade CCDs, CTE values are very close to 1, typically 99.999%.

3. Quantum efficiency (QE)

The quantum efficiency gives the ratio of the number of photons detected by the CCD to the total number of incoming photons. The QE of back- and front-illuminated cameras can be estimated by means of the following simple formulas [3]:

$$QE_{BI}(E) = CCE(1 - R(E)) (1 - e^{-x_{Si}/L_A(E)}), \quad (1)$$

or:

$$QE_{FI}(E) = CCE(1 - R(E)) (e^{-x_{SiO_2}/L_A(E)} (1 - e^{-x_{Si}/L_A(E)}), \quad (2)$$

where R is the reflection coefficient for silicon, CCE the charge collection efficiency and x_{Si} and x_{SiO_2} the thicknesses of the depletion region and dead layer, respectively. The absorption length L_A is the inverse of the total photon attenuation coefficient for Si. R and L_A depend on the energy of the incoming photons.

4. Dark current

The dark current originates from thermal electron excitations. It strongly depends on the temperature of the CCD chip. For Si, the dark current decreases by a factor 2 for every diminution of the temperature by 6° C [13].

It can be noted that the surface dark current is significantly smaller in multi-pinned phase (MPP) CCDs [14], a category of devices to which belongs the back-illuminated CCD used in the present study.

5. Readout noise

The total CCD noise consists mainly of the above-mentioned dark current noise and the so-called readout noise (RN). The RN is the noise that is measured at the output of the CCD camera system in the absence of any source of radiation. It originates from the electronics of the CCD camera, being mainly

due to the ADCs. Note that the contribution of the dark current to the CCD noise increases linearly with the CCD exposure time, whereas the readout noise does not depend on the exposure time.

III. EXPERIMENTAL SET-UP

A. Von Hamos spectrometer

To characterize the two CCD cameras as a function of the x-ray energy, monochromatic x-ray radiations were needed between 1 keV and 18 keV. A simple solution would have consisted to irradiate the CCD detectors with monochromatized synchrotron radiation but the high intensity of synchrotron radiation beams (typically 10^{10} – 10^{12} photons per mm^2) was inadequate for the foreseen characterization measurements. In particular, single events per pixel were required, which was hardly feasible with synchrotron radiation. The characteristic x-ray emission lines of a variety of elemental and compound samples were therefore chosen as sources of monochromatic radiation. The fluorescence x-ray emission was produced by irradiating the samples with the bremsstrahlung of x-ray tubes. In order to probe the performances of the CCD detectors with well resolved $K\alpha$, $K\beta$, $L\alpha$ and $L\beta$ transitions, the characteristic x-ray emission lines from the samples were first filtered with a wavelength dispersive in-

strument, namely a crystal spectrometer, before being measured by the CCD cameras. Actually, as the two CCDs were planned to serve as x-ray detectors for this crystal spectrometer, the set-up represented some kind of a natural choice.

The measurements were performed at the University of Fribourg, Switzerland, by means of a high-resolution von Hamos-type bent crystal spectrometer, employing either the back-illuminated CCD or the front-illuminated one for the detection of the x-rays diffracted by the crystal. A schematic drawing of the spectrometer geometry is presented in Fig.2. A more detailed description of the instrument can be found in [15]. The resolving power of the von Hamos spectrometer depends mainly on the width of the x-ray source. In order to obtain relative energy resolutions $\Delta E/E$ of about 10^{-4} , the width of the radiation source should be of the order of a few tenths of millimeter. For this reason, the sample was viewed by the crystal through a narrow rectangular slit placed between the sample and the crystal. The slit consisted of two juxtaposed 1 mm thick Ta plates. The slit width was adjustable by means of a micrometer screw. By decreasing the slit width the resolution of the spectrometer is improved but its efficiency diminishes. For the present measurements a slit width of 0.4 mm was chosen, which represented the best compromise

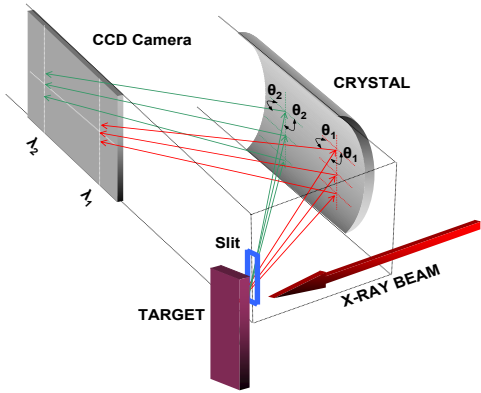


FIG. 2: Schematic drawing of the von Hamos geometry.

between a high enough luminosity of the spectrometer and an acceptable energy resolution (about 5×10^{-4}). From the energy calibration of the spectrometer, a relative precision better than 100 ppm was found for the energies of the measured characteristic lines, while for the measured intensities uncertainties of about 5% were obtained.

B. X-ray tubes

Two different 100 kV/3 kW Coolidge-type x-ray tubes were used. The first one equipped with a scandium anode and a $150 \mu\text{m}$ beryllium window was employed for the measurements between 1 keV and 3.6 keV. For the measurements of higher energy x-ray lines, a gold anode x-ray tube with a $1000 \mu\text{m}$ beryllium window was used. For the same currents and voltages, the characteristic x-ray emission of the samples was indeed found to be

more intense below 3.6 keV with the scandium x-ray tube, due to its thinner beryllium window. Depending on the samples and the measured transitions, the two x-ray tubes were operated at high-voltages between 20 kV and 60 kV and currents between 10 mA and 30 mA.

C. Crystals

The Bragg angle domain covered by the von Hamos spectrometer extends from 24° to 61° . In order to measure x-rays with energies ranging between 1 keV and 18 keV, five different crystals were employed. The crystal specifications and energy range covered by each crystal in first order of reflection are given in Table I. As shown, covered energy ranges are overlapping for all crystals except for the two first ones where there is an energy gap between 1.160 keV and 1.645 keV which is not accessible in 1st order of reflection with the quoted crystals. For this reason the $K\alpha_1$ x-ray lines of Mg and Al (1.254 keV and 1.487 keV respectively) were observed in 2nd order of reflection, using the TIAP crystal. The same holds for the x-ray lines above 16.836 keV, as for instance the $K\alpha_1$ transition of Mo (17.479 keV), that were measured in 2nd order, too, but with the SiO_2 ($\overline{2}\overline{2}\overline{3}$) crystal.

TABLE I: Characteristics of the employed crystals

Crystal	2d (Å)	Energy range (keV)
TlAP (001)	25.772	0.547–1.160
SiO ₂ (1 $\bar{1}$ 0)	8.5096	1.645–3.563
LiF (200)	4.0280	3.475–7.528
SiO ₂ (2 $\bar{2}$ 3)	2.7500	5.090–11.026
LiF (420)	1.8010	7.772–16.836

D. Irradiated samples

Most irradiated samples were high-purity (better than 99%) metallic foils or polycrystalline plates mounted on aluminum frames. Some powder samples, like SrTiO₂ used for the measurements of the Sr L α and L β lines, were prepared by dusting the material onto adhesive aluminium backings. Samples were 1.5 cm wide and 2.5 cm high, with thicknesses varying from 4 μ m to 50 μ m. For the Ar and Kr gaseous samples, a 10 mm in-diameter cylindrical gas cell was employed. For both gases, the pressure inside the cell was 1 bar. To minimize the absorption of the incoming and outgoing photons and diminish the background resulting from the visible light produced by the irradiated gases, the irradiation and exit windows of the cell were made of 25 μ m thick black Kapton foils. The list of all employed samples is given in Table II.

In order to obtain reliable results for the ratios of the CCD efficiencies, the same samples were used for the measurements performed with the back- and front-illuminated cameras. The same holds for the x-ray tube

parameters and the employed crystals. This way the corrections for the sample x-ray fluorescence yield production, self-absorption in the sample of the incoming and outgoing x-ray radiation, solid angle of the spectrometer and crystal reflectivity could be omitted in the data analysis.

E. Charge coupled devices

The main specifications of the employed front-illuminated (FI) and back-illuminated (BI) CCDs are quoted in Table III where the chip size, pixel resolution, depletion depth, readout noise and full well capacity are given. Photographs of the two cameras are presented in Fig.3 and Fig.4. Both chips (front illuminated: LCX-TE/CCD-1024E1; back illuminated: MTE400B E2V MPP CCD 36-10) were manufactured by EEV [11] for Roper Scientific [9] which provides complete CCD systems and related control electronics and software.

The CCDs were operated through a dedicated controller (ST-133 from Roper Scientific) at a rate of 1 MHz for the back-

TABLE II: Measured x-ray emission lines

Energy ^a (eV)	Element	Emission line	X-ray tube kV/mA	Crystal	Reflection order	Target
1040.98	Na	$K\alpha_1$	Sc 30/20	TlAP(001)	1	NaCl powder
1253.6	Mg	$K\alpha_1$	Sc 30/20	TlAP(001)	2	metallic
1486.7	Al	$K\alpha_1$	Sc 30/20	TlAP(001)	2	metallic
1557.45	Al	$K\beta_1$	Sc 30/20	TlAP(001)	2	metallic
1739.98	Si	$K\alpha_1$	Sc 30/15	$\text{SiO}_2(1\bar{1}0)$	1	polysilicon
1806.56	Sr	$L\alpha_1$	Sc 30/20	TlAP(001)	2	SrTiO ₃ powder
1835.94	Si	$K\beta_1$	Sc 30/15	$\text{SiO}_2(1\bar{1}0)$	1	polysilicon
1871.72	Sr	$L\beta_1$	Sc 30/20	TlAP(001)	2	SrTiO ₃ powder
2013.7	P	$K\alpha_1$	Sc 30/20	$\text{SiO}_2(1\bar{1}0)$	1	powder
2139.1	P	$K\beta_1$	Sc 30/20	$\text{SiO}_2(1\bar{1}0)$	1	powder
2307.84	S	$K\alpha_1$	Sc 30/15	$\text{SiO}_2(1\bar{1}0)$	1	powder
2464.04	S	$K\beta_1$	Sc 30/15	$\text{SiO}_2(1\bar{1}0)$	1	powder
2622.39	Cl	$K\alpha_1$	Sc 30/15	$\text{SiO}_2(1\bar{1}0)$	1	KCl crystal
2815.6	Cl	$K\beta_1$	Sc 30/15	$\text{SiO}_2(1\bar{1}0)$	1	KCl crystal
2957.7	Ar	$K\alpha_1$	Sc 30/20	$\text{SiO}_2(1\bar{1}0)$	1	gas
3190.5	Ar	$K\beta_1$	Sc 30/20	$\text{SiO}_2(1\bar{1}0)$	1	gas
3313.8	K	$K\alpha_1$	Sc 30/10	$\text{SiO}_2(1\bar{1}0)$	1	KCl crystal
3589.6	K	$K\beta_1$	Sc 30/10	$\text{SiO}_2(1\bar{1}0)$	1	KCl crystal
3691.68	Ca	$K\alpha_1$	Au 20/10	LIF(200)	1	metallic
4012.7	Ca	$K\beta_1$	Au 40/10	LIF(200)	1	metallic
4090.6	Sc	$K\alpha_1$	Au 20/10	LIF(200)	1	metallic
4460.5	Sc	$K\beta_1$	Au 30/10	LIF(200)	1	metallic
4510.84	Ti	$K\alpha_1$	Au 20/10	LIF(200)	1	metallic
4931.81	Ti	$K\beta_1$	Au 30/10	LIF(200)	1	metallic
4952.2	V	$K\alpha_1$	Au 20/10	LIF(200)	1	metallic
5414.72	Cr	$K\alpha_1$	Au 30/15	$\text{SiO}_2(2\bar{2}3)$	1	metallic
5427.29	V	$K\beta_1$	Au 30/10	LIF(200)	1	metallic
5898.75	Mn	$K\alpha_1$	Au 30/10	$\text{SiO}_2(2\bar{2}3)$	1	metallic
5946.71	Cr	$K\beta_1$	Au 30/25	$\text{SiO}_2(2\bar{2}3)$	1	metallic
6403.84	Fe	$K\alpha_1$	Au 30/10	$\text{SiO}_2(2\bar{2}3)$	1	metallic
6490.45	Mn	$K\beta_1$	Au 30/10	$\text{SiO}_2(2\bar{2}3)$	1	metallic
6930.32	Co	$K\alpha_1$	Au 30/10	$\text{SiO}_2(2\bar{2}3)$	1	metallic
7057.98	Fe	$K\beta_1$	Au 30/10	$\text{SiO}_2(2\bar{2}3)$	1	metallic
7478.15	Ni	$K\alpha_1$	Au 30/15	$\text{SiO}_2(2\bar{2}3)$	1	metallic
7649.43	Co	$K\beta_1$	Au 30/10	$\text{SiO}_2(2\bar{2}3)$	1	metallic
8047.78	Cu	$K\alpha_1$	Au 30/15	$\text{SiO}_2(2\bar{2}3)$	1	metallic
8264.66	Ni	$K\beta_1$	Au 40/30	$\text{SiO}_2(2\bar{2}3)$	1	metallic
8638.86	Zn	$K\alpha_1$	Au 30/20	$\text{SiO}_2(2\bar{2}3)$	1	metallic
8652.5	Re	$L\alpha_1$	Au 50/20	LIF(420)	1	metallic
8905.29	Cu	$K\beta_1$	Au 40/30	$\text{SiO}_2(2\bar{2}3)$	1	metallic
9175.1	Ir	$L\alpha_1$	Au 30/20	$\text{SiO}_2(2\bar{2}3)$	1	metallic
9572	Zn	$K\beta_1$	Au 30/20	$\text{SiO}_2(2\bar{2}3)$	1	metallic

^afrom [16]

TABLE II: Continuation.

Energy ^a (eV)	Element	Emission line	X-ray tube kV/mA	Crystal	Reflection order	Target
9713.3	Au	L α_1	Au 50/30	LIF(420)	1	metallic
10010	Re	L β_1	Au 60/30	LIF(420)	1	metallic
10543.72	As	K α_1	Au 50/30	LIF(420)	1	ZnAs powder
10708.3	Ir	L β_1	Au 30/20	SiO ₂ (2 $\bar{2}$ 3)	1	metallic
11222.4	Se	K α_1	Au 40/15	LIF(420)	1	powder
11442.3	Au	L β_1	Au 60/30	LIF(420)	1	metallic
11726.2	As	K β_1	Au 60/30	LIF(420)	1	ZnAs powder
12495.9	Se	K β_1	Au 50/30	LIF(420)	1	powder
12649	Kr	K α_1	Au 60/30	LIF(420)	1	gas
14112	Kr	K β_1	Au 60/30	LIF(420)	1	gas
15775.1	Zr	K α_1	Au 60/30	SiO ₂ (2 $\bar{2}$ 3)	2	metallic
17479.34	Mo	K α_1	Au 60/30	SiO ₂ (2 $\bar{2}$ 3)	2	metallic

^afrom [16]

illuminated camera and 100 kHz for the front-illuminated one, which corresponded to read-out times of 0.6 sec., respectively 2.6 sec., for full images and 16 bit signals per pixel. As both CCDs were used in the full frame mode, the cameras should be shielded from the incoming radiation during the readout operations. This was done with an x-ray shutter placed in front of the detector. The shutter which was developed for the von Hamos spectrometer consists of two superimposed metallic absorbers, a 0.5 mm thick stainless steel plate in the front and a 1.5 mm Al plate behind. During data collection, both plates move apart from the longitudinal axis of the CCD which coincides with the dispersive axis of the crystal spectrometer (see Fig. 3b). The signals delivered by the controller to start and stop the data acquisition are also employed

to open, respectively close, the x-ray shutter. For this reason and because the time for opening and closing the shutter is 0.21 sec, the central area of the CCD is exposed a little bit longer than the top and bottom parts.

For both cameras, the CCD chip sits on a cold finger which is mounted on a thermoelectric two-stage Peltier cooler. The Peltier elements are cooled down with a circulation of water at 5°C. In order to diminish the dark current noise, for the present experiment the CCD chips were operated at -50°C. In addition, to minimize the remanent pixel charges a dedicated cleaning procedure (*Clean Circles function*) was applied before each new frame acquisition. This function shifts the self-accumulated charges in the CCD array to the serial register and then discards them.

The data were collected in the so-called multiple-frame mode. Depending on the intensity of the measured characteristic x-rays, the number of acquired images varied between 200 and 2000 with exposure times of 1–5 sec. per image. The latter were chosen as a function of the number of photons impinging on the CCD in order to avoid multiple hits in a single pixel. In order to get rid of the own CCD dark charge pattern, a background image, which was recorded beforehand with the x-ray shutter closed, was subtracted from all acquired frames. After the subtraction of the background frame, all images corresponding to the same measurement were stored in a single file with the possibility of viewing or processing off-line any individual frame.

Both CCDs were operated in the Full Speed-Free Run mode which is used for real-time sequential acquisitions of data. In this mode data collection is steered directly by the CCD hardware (controller) without any interaction with the computer. In the Free Run timing mode the shutter opens when the readout of the previous frame is completed, closes again after the preset exposure time, remains closed during the data readout and then opens again for the acquisition of the next image. This measuring cycle is repeated until the chosen number of frames is reached. Each new acquired image, after subtraction of the background frame, is displayed on the PC

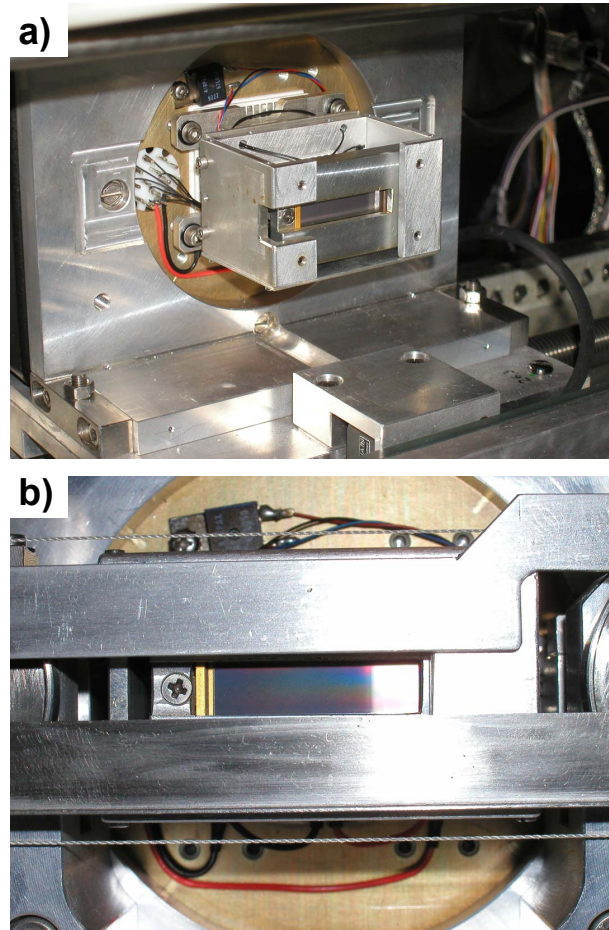


FIG. 3: Photographs of the FI camera. a) The camera as installed on its moveable support. b) Zoom on the CCD chip and x-ray shutter.

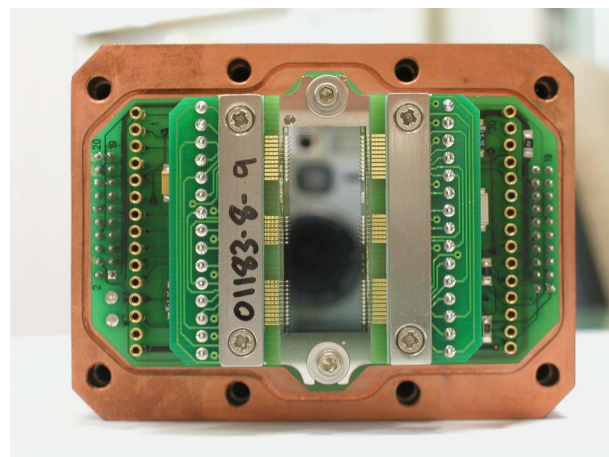


FIG. 4: Photograph of the BI camera chip.

TABLE III: CCD characteristics

	Front illuminated	Back illuminated
Chip size	1024×256	1340×400
Pixel size	$27 \times 27 \mu\text{m}^2$	$20 \times 20 \mu\text{m}^2$
Depletion depth	$50 \mu\text{m}$	$\sim 15 \mu\text{m}$
Readout noise	$3\text{--}7 e^-$ at 100 kHz	$8.5 e^-$ at 1MHz
Full well capacity	$348 ke^-$	$201 ke^-$

screen, which permits to have a live survey of the measurements.

IV. DATA ANALYSIS

A. 2D charge pattern

As a result of the interaction of the incoming x-rays with the Si epitaxial layer electron-hole pairs are created. The number N of released electrons for the full absorption of an x-ray of energy E is given by:

$$N = \frac{E(\text{eV})}{3.65}, \quad (3)$$

where the value of 3.65 eV corresponds to the first ionization potential of silicon.

The released electrons are captured in the pixel potential wells and the corresponding trapped charges generate electronic signals which after amplification are converted into digital numbers. Representing these numbers by specific colors, a two-dimensional image can be constructed which reflects the charge pattern of the CCD as a result of its exposure to the x-ray radiation. In such images, the coordinates of the point correspond to the

row and column numbers of the pixel and the color to the charge that was deposited in that pixel. Since the charge deposited in the pixels is proportional to the energy of the absorbed photons, good pixels can be sorted by filtering the data with an energy window. If the pixel charge fulfills the conditions of the energy window, a one is assigned to that pixel, if not a zero. This procedure permits to diminish the number of background events originating from scattered photons, photons diffracted in higher orders by the crystal or cosmic rays. The energy window can be determined from the frequency distribution of the charges deposited in the pixels. This distribution called histogram can be also used advantageously to probe the CCD performances or determine its characteristics. A more detailed description of the histograms and image filtering procedure is given in the next section.

In measurements performed with the von Hamos spectrometer the two-dimensional images corresponding to single exposures of the CCD are first filtered, using the adequate energy window, and then summed together. Thanks to the spatial resolution of the CCD

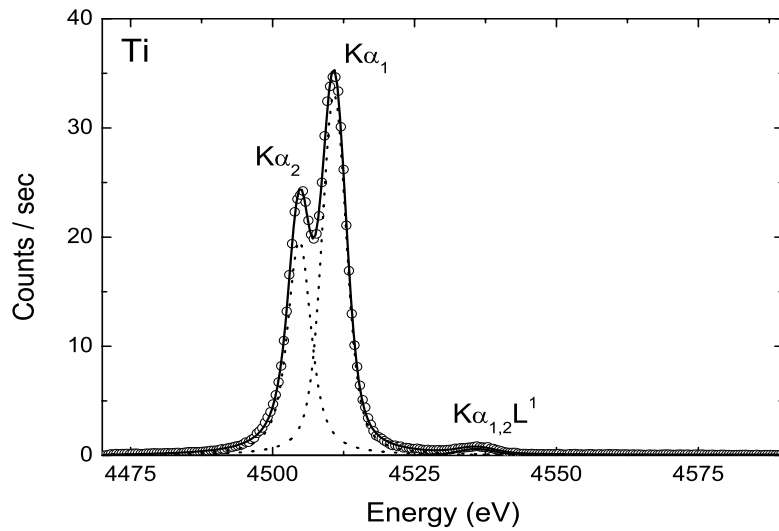


FIG. 5: High-resolution $K\alpha$ x-ray spectrum of Ti measured with the von Hamos spectrometer equipped with the FI camera.

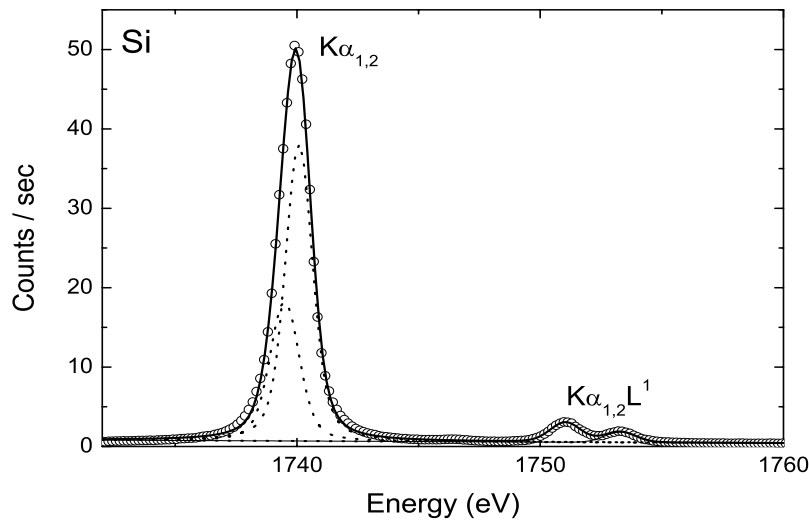


FIG. 6: High-resolution $K\alpha$ x-ray spectrum of Si measured with the von Hamos spectrometer equipped with the BI camera.

detector, the resulting total image presents vertical stripes corresponding to the different wavelengths, i.e., energies, of the x-ray radiation diffracted by the crystal according to the Bragg law. To obtain the corresponding high-resolution x-ray spectrum, the total image is finally projected onto the dispersive

axis of the spectrometer which is parallel to the length direction of the CCD. For illustration, the high-resolution $K\alpha$ x-ray spectra of Ti and Si measured with the FI and BI cameras, respectively, are shown in Fig.5 and Fig.6. The resolved weak x-ray structures occurring in these spectra at about 4535 eV and

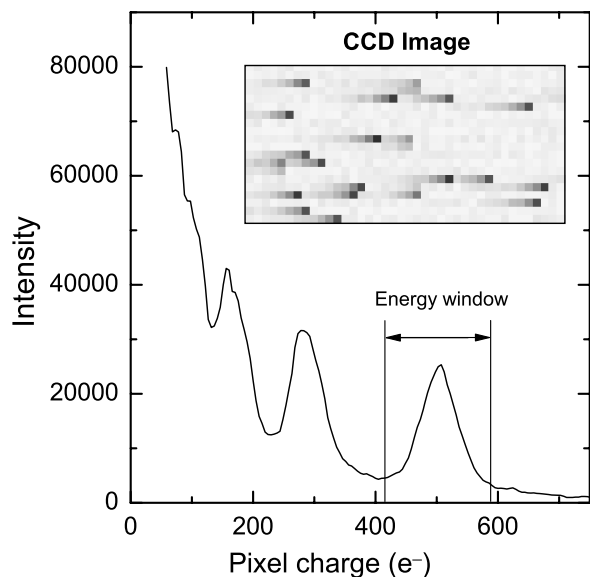


FIG. 7: Histogram of the charge distribution in the FI CCD. The histogram was constructed from the measurement of the Ti $K\alpha$ x-ray spectrum. In the inset, a selected area of a 2D image is shown.

1752 eV correspond to the 1st order L satellites of the $K\alpha$ transitions, i.e., to the 2p–1s transitions with one additional spectator vacancy in the L-shell.

B. CCD histograms

In Figs.7 and 8 two examples of histograms are presented. Selected areas of the corresponding 2D CCD images are shown in the insets. The histograms correspond to the above-mentioned Ti $K\alpha$ and Si $K\alpha$ measurements. In both histograms, pixel charges are expressed in e^- . The conversion factor between the digital numbers given by the ADCs and the corresponding pixel charges in e^- was

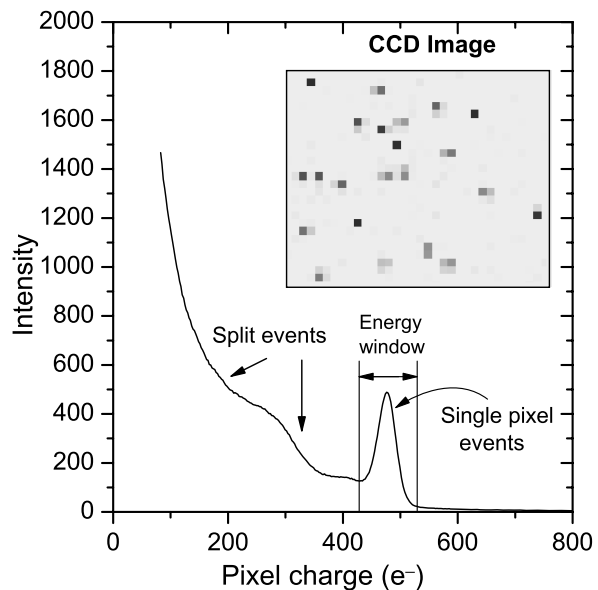


FIG. 8: Histogram of the charge distribution in the BI CCD. The histogram was constructed from the measurement of the Si $K\alpha$ x-ray spectrum. In the inset, a selected area of a 2D image is shown.

determined using Eq.(3) and the energy responses of the CCDs discussed at the end of this section.

The 2D image of the FI camera shows that each event consists of a main pixel accompanied by a horizontal tail of several pixels on the left. This "tailing" effect appears in the corresponding histogram as a series of peaks shifted to lower charge values. A similar observation reported in [3] was explained by a poor charge transfer efficiency due to a "design trap" problem. We have found that independently on the measured x-ray energy, the positions of the secondary peaks are always shifted down by a factor of about 0.6 with respect to the next peak above. The

length of the tails is always the same, no matter on which part of the CCD the photon is absorbed but for increasing photon energies the tail length grows. This implies that the "design trap" should be located between the last polysilicon gate (transfer gate) and the serial register. A plausible explanation for the charge tailing is that the ends of the channel stops on the side of the serial register were designed wider in order to better guide the charges to the register. Due to that, a small potential difference between the last gate and the transfer gate occurs which can hold back several hundreds of electrons [3]. Note that the observed tails are horizontal because for the FI camera the serial register is vertical. As indicated by the histogram, in our case the percentage of electrons trapped by this parasitic potential is about 60%. In other words, only 40% of the charge deposited originally in the hit pixel is forwarded to the controller. During the next transfer 40% of the "delayed" charge, i.e., 24% of the original one, will be assigned by the controller to the next pixel although the latter had no charge in the real CCD image. This erroneous attribution of charges to empty pixels during the readout process continues until the wrong signals become negligibly small and disappear in the noise. To determine the real charge deposited on the single hit pixel (the one with the biggest charge), one should thus sum the

charges of all neighbor pixels belonging to the "trailing" event.

A completely different behavior is observed for the BI camera. As shown by the inset of Fig.8, in this case the charges are either deposited in single pixels or split randomly between several neighbor pixels. This charge splitting effect [3] occurs when a photon is absorbed in the field free region (see Fig.1a). Due to the weak electric field existing in this region, the electron cloud can indeed diffuse over an area corresponding to several pixels before being trapped by the potential wells of different pixels. Therefore, the corresponding histogram contains a small peak which corresponds to the single event pixels and a broad structure arising from the split events. Of course, the image filtering process can be performed using an energy window corresponding to the single event peak of the histogram [7] but this leads to a significant loss in the detection efficiency. It can be noted here that split event pixels are rarely observed in images taken with the FI camera, except for the highest photon energies. This is due to the design of the FI CCD in which the field free region is located opposite the exposed side of the chip, after the depletion region. As a consequence, only few x-rays and only those with a high enough energy can reach the field free region where the charge splitting takes place.

In order to recover the charges lost as a

result of the tailing and splitting effects observed with the FI and BI cameras, dedicated image processing codes were developed. For the images taken with the BI camera, the code determines first the average charge of the single event pixels. Then the charges corresponding to the split event pixels are summed up with the condition that the obtained sum should be consistent within the experimental uncertainty with the average charge of the single event pixels. Finally the total charge is assigned to the pixel with the highest partial charge. As in most examined 2D images, the major part of the charge was found to be shared between 4 neighbor pixels or less, a maximum of 4 pixels is taken into consideration by the code in the sum of the split charges. For FI images, a similar code was developed. In this case, the charges of the tail pixels are summed and the total charge assigned to the first pixel on the right of the tail. If split event pixels are present, their charge is accounted for in the sum. For illustration, selected areas of raw and processed 2D images are shown for both cameras in Fig.9.

The drastic improvements brought by the two image processing codes are illustrated by the Figs.10 and 11, where the histograms before (red line) and after (blue line) correction are shown. In Fig.10, the histogram of the raw data corresponding to the measurement of the P $K\alpha$ x-ray line performed with the BI

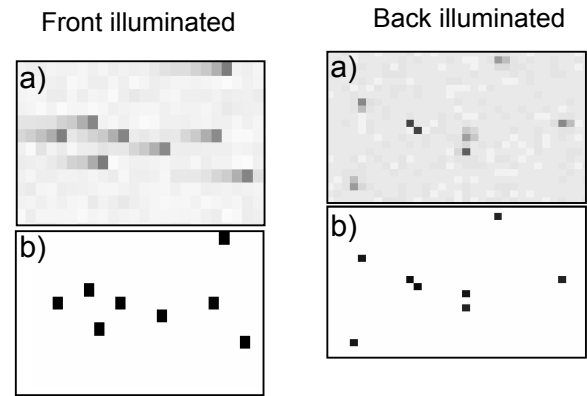


FIG. 9: Selected areas of raw and corrected images of the FI and BI cameras.

camera does not show any significant single event peak that could be assigned to the $K\alpha$ transition of phosphorus. Actually, the small peak observed at about $480 e^-$ corresponds to the $K\alpha$ transition of silicon. According to Eq.(3), this Si transition is indeed expected at $477 e^-$. As the energy of the P $K\alpha$ x-rays lies just above the K-shell ionization energy of silicon, the weak peak is due to the self-absorption in the epitaxial layer of the Si $K\alpha$ x-rays induced by photoionization in the CCD material by the incoming characteristic x-rays of phosphorus. However, as shown by the blue line in Fig.10, the single event peak corresponding to the P $K\alpha$ line is clearly resolved after correction of the raw data with the above-mentioned image processing code. The fitted peak position (at $504 e^-$) corresponds satisfactorily to the theoretical value of $551 e^-$ given by Eq.(3). The difference arises from events that were split into more than 4 pixels, i.e., from the residual charges

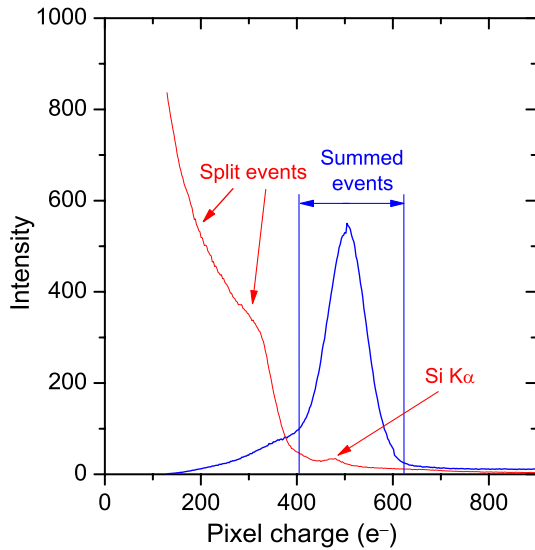


FIG. 10: Histogram of the charge distribution in the BI CCD resulting from the measurement of the P $K\alpha$ x-ray spectrum. The red line corresponds to the histogram of raw data, the blue one to the histogram of corrected data (for details, see the text).

that were not considered by the code in the computation of the total charge. Actually, the asymmetry occurring on the low-charge side of the peak is due to the charges of these omitted pixels.

As shown in Fig.11 where the histogram corresponding to the measurement of the $K\alpha$ transition of aluminium is depicted, the correction software for images collected by means of the FI CCD is especially useful for low energy x-rays. In the uncorrected histogram (red line), the Al $K\alpha$ peak corresponding to the pixels with the largest charge is partly overlapping with the tail of the electronic noise and with the peak associated to

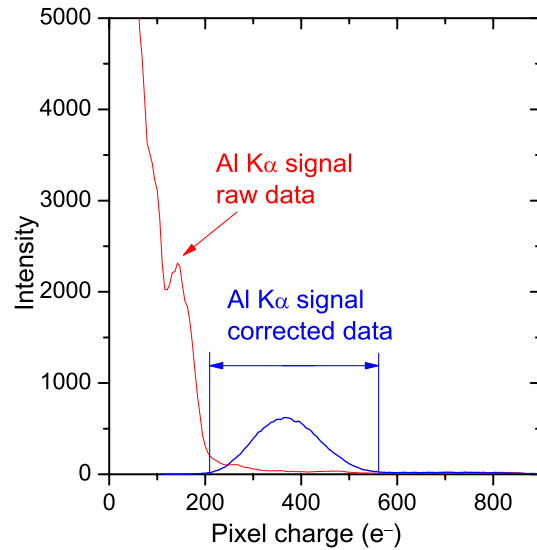


FIG. 11: Histogram of the charge distribution in the FI CCD resulting from the measurement of the Al $K\alpha$ x-ray spectrum. The red line corresponds to the histogram of raw data, the blue one to the histogram of corrected data (for details, see the text).

the first pixels on the left, i.e. the pixels with the second highest charge. Usually a width of 3σ is chosen for the energy window. However, if such a width is employed for filtering the unprocessed images, noise events will be sorted as good events with the result of a strong increase of the background in the high-resolution x-ray spectrum. On the other hand, the use of a narrower energy window leads to a significant loss of good events, i.e., to a diminution of the intensity of the transition of interest in the high-resolution x-ray spectrum. No such difficulty is encountered with the corrected histogram (blue line) in which a single peak is observed which is

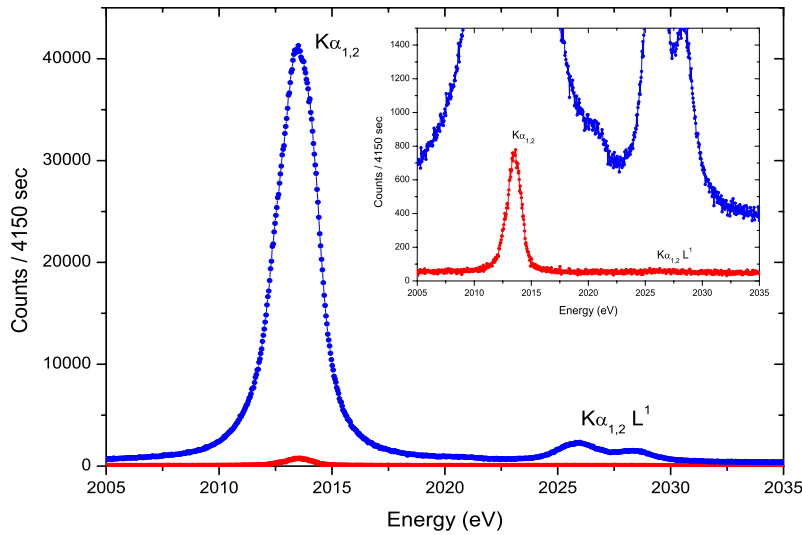


FIG. 12: High-resolution K x-ray spectrum of phosphorus measured with the von Hamos spectrometer equipped with the BI CCD camera. Red points stand for the raw spectrum, blue ones for the spectrum obtained after correction of the 2D images with the code discussed in the text. As shown in the inset, the x-ray satellite structure between 2022 eV and 2032 eV cannot be resolved from the background in the uncorrected spectrum.

well resolved from the electronic noise. The centroid position found for the peak is $373 e^-$, in good agreement with the value of $407 e^-$ obtained from Eq.(3).

The two developed image processing codes permit to improve in a very significant way the histograms of both CCDs and to use then well defined energy windows for the image filtering. An example of the improvement brought by the correction software to the final x-ray spectra is shown in Fig.12 for the BI camera. The price to pay for this improvement is some deterioration of the energy resolution of the CCDs. Comparing for instance the relative resolution of the peaks presented in Figs.7 and 11 (FI camera), respectively in Figs.8 and 10 (BI camera), one sees indeed that the relative charge or energy resolution becomes worse by a factor of about

3 for the FI camera and a factor of about 2 for the BI camera after the image processing. This worse resolution implies the use in the data analysis of wider energy windows, which in turn results in some enhancement of the background in the final high-resolution x-ray spectra. The main reason for the resolution loss resides in the fact that in the correction process the uncertainties on the charges of all summed pixels are added together.

The above discussed charge trailing and charge splitting effects would make difficult the use of the two CCDs for the direct measurement of a polychromatic x-ray source. In particular, low x-ray energy spectra would be hardly measurable. Due to the presence of different energies in the incoming x-rays, many peaks would be indeed overlapping in the histograms, which would make hopeless

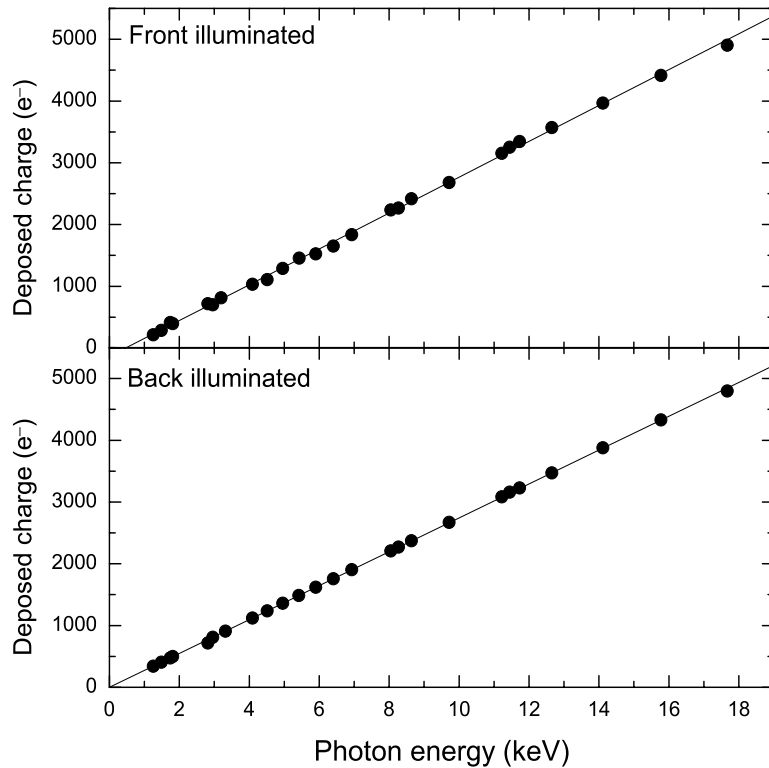


FIG. 13: Charge deposited in the two CCDs as a function of the measured photon energy. Experimental values are represented by full circles. Both sets of measured data were fitted with a linear function (solid line).

the use of correction codes as those presented above. In this case, the single possibility would consist to choose an energy window corresponding to the peak of the single event pixels for the BI camera and the peak of the pixels with the highest charge for the FI camera with the result, however, that the efficiency of the two CCDs would then decrease dramatically.

To determine the energy response of the two CCDs, the $K\alpha$ transitions of a variety of elements ranging from Mg ($E=1.254$ keV) to Mo ($E=17.479$ keV) were measured with the von Hamos spectrometer. The obtained 2D

images were corrected to account for the tail and split events and for each measurement the corresponding histogram was constructed. The centroid positions of the resolved charge peaks occurring in the histograms were determined by means of a least-squares fitting procedure, using for each peak a single Gauss function. Results are plotted as a function of the transition energy in Fig.13. As shown, the experimental points could be well fitted with straight lines, showing that the energy response of both CCDs is linear over the energy range 1 keV–18 keV. The slopes found for the straight lines are $274 e^-/\text{keV}$ (BI) and

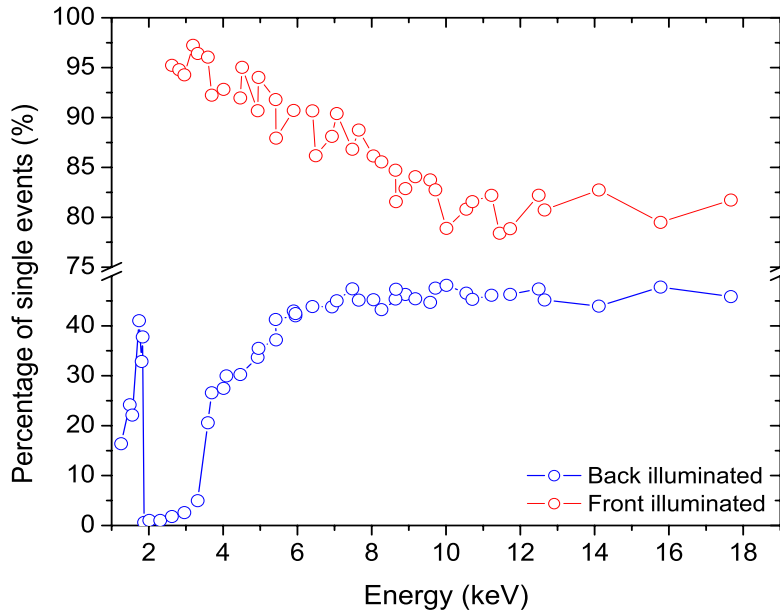


FIG. 14: Percentages of events detected in a single pixel as a function of the incoming photon energy. Orange open circles stand for FI data, blue ones for BI data.

295 e^- /keV (FI). Noticing that the inverse of the slope should correspond to the first ionization potential of Si, values of 3.65 eV and 3.39 eV are found for the BI and FI cameras, respectively. The deviation of about 7% observed for the FI camera is probably due to the fact that split events and tail events with the smallest charges were not considered by the correction code for the FI CCD. For the same reason, the FI straight line does not converge exactly to the origin.

From these measurements, the average value of the CCD noise was also determined. Results of 31.1 e^- (FI) and 28.7 e^- (BI) were found. They correspond to the FWHM of the noise event histograms. Both values are bigger than the noise levels given in the CCDs specifications (see Table III). That in-

creased noise is principally due to the presence in the vicinity of the CCDs of a turbo-pump and several stepping motors. From the above noise levels and other considerations related to the obtained histograms, we have estimated for each camera the lowest energy that can be measured with the von Hamos spectrometer. Low energy limits of 950 eV for the FI camera and 450 eV for the BI one were obtained.

C. Charge splitting effect

The photon energy dependence of the charge splitting effect was determined for both CCD cameras. The results are presented in Fig.14. As shown, the relative number of single pixel events varies as a function of the

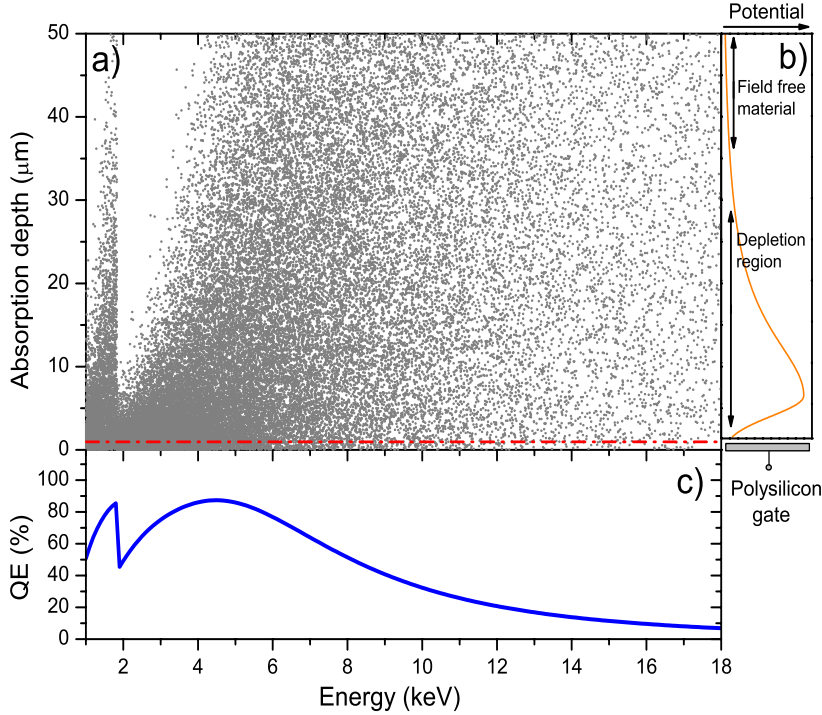


FIG. 15: Results of Monte Carlo simulations of photon absorption in the FI CCD. a) Depth absorption as a function of the photon energy (each point corresponds to an absorption event). b) Schematic variation of the electrostatic field across the pixel depth. c) Ideal quantum efficiency derived from the simulations.

photon energy in an opposite way for the two CCDs. It can be seen that for the FI camera almost all of the detected events are confined to a single pixel for low energy x-rays. When the photon energy increases, a slight decrease in the relative number of single event pixels is observed. At the highest measured energy (17.479 keV) about 20% of all events are split between 2 to 4 pixels. The number of single event pixels could not be determined for energies below 2 keV due to the poor charge transfer efficiency resulting in split charge loss in the background noise. A different behav-

ior of the charge splitting effect can be seen for the BI CCD. In the photon energy range from 1 keV to 1.84 keV (K-absorption edge of Si) an increase in the number of detected single event pixels is observed. For x-ray energies just above 1.84 keV the number of single event pixels decreases drastically to a very low level of less than 1% of the total number of detected events. This fact signifies that almost all events are split across several pixels. When the x-ray energy is further increased the number of single events increases and for energies above 6 keV the ratio of the single

events to the split events reaches a constant level of 45%.

To better understand the photon energy dependence of the charge splitting effect Monte Carlo simulations of the photon absorption in the CCDs were performed. Results are presented in Fig.15a for the FI camera and in Fig.16a for the BI one. The Monte Carlo simulations were computed employing an exponential probability distribution [3]:

$$x_i = -L_x(E)\log_e(N_r), \quad (4)$$

where $L_x(E)$ is the absorption length in silicon for a given x-ray energy and N_r a random number between 0 and 1. The calculated x_i correspond to the depth at which a photon of given energy is fully absorbed as a result of the photoelectric effect. The computation was performed with a 10 eV photon energy step and for each step 1000 events were generated.

In Figs.15b–16b the schematic pixel potential well profiles are shown (orange lines). Depending on the strength of the electric field two regions can be distinguished: a field free material and a depletion region. By design, in case of front-side photon illumination, photons fall on the front surface where the gates are located, whereas on the contrary for back-side photon illumination x-rays enter the back-surface farthest from the gates.

Therefore, with respect to the direction of incident photons, these regions are located in an opposite way for FI and BI cameras. As already discussed in Sec.II, for the FI camera x-rays penetrating the gate and oxide structure (marked as a red dashed line in Fig.15a) may be absorbed before entering the depletion region and the field free material. In the case of the BI camera, x-rays enter the field free material first and then the depletion region. From the Monte Carlo simulations for the BI camera one can see that for photon energies slightly above the K-absorption edge of Si (i.e 1.84 keV) almost all x-rays are absorbed within a depth of 3–4 μm where the electric field is weak. Therefore, at these energies most of the generated electrons can diffuse thermally to neighboring pixels before being trapped in the potential well of one pixel. This assertion agrees with the results presented in Fig.14, where for energies just above 1.84 keV the number of single events is close to zero. As the photon energy increases photon absorption takes place directly in the depletion region.

For the FI camera, our experimental results for the degree of charge splitting as a function of the photon energy are also confirmed by Monte Carlo simulations. At low energies almost all of the incident x-ray photons are absorbed directly in the depletion region where the electric field is strong enough

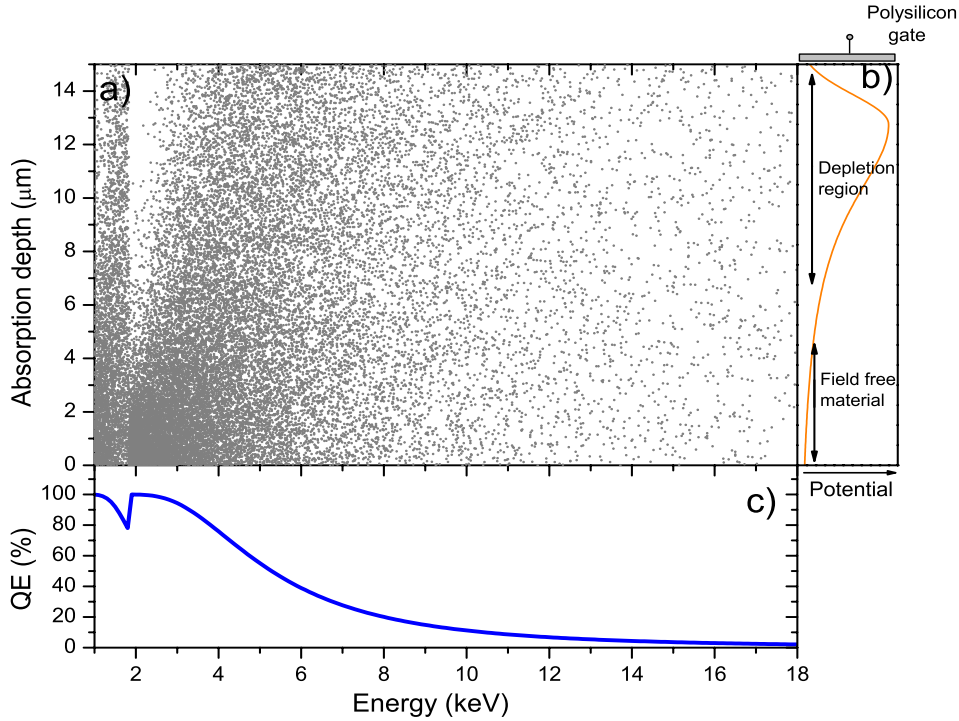


FIG. 16: Same as Fig.15 but for the BI CCD.

to prevent thermal diffusion of the electron cloud. Therefore, in comparison with the BI CCD, the charge splitting effect is weak. However, the number of split charge events increases at higher photon energies due to the larger penetration depth. As a result, photo-absorption takes place beneath the depletion region, where again due to the weak electric field the charge can diffuse to adjacent pixels.

D. Quantum efficiency ratio of the front- and -back illuminated CCDs

In Fig.15c and Fig.16c the ideal quantum efficiency as a function of incoming photon

energy is shown. The QE curves were calculated employing the analytical formulas (1–2) and using the absorption coefficients reported in [17] in the energy range between 1 keV and 18 keV. We assumed that the CCE is equal to one and that there are no losses due to photon reflection on the Si chip surface. In fact, theoretical QE curves were also deduced from the Monte Carlo simulation by summing the events which were absorbed within a depth of 50 μm for the FI camera and 15 μm for the BI camera. The calculated QE curves show two important characteristic features. First, as the photon energy approaches the K-absorption edge of Si a completely different

behavior in the QE of the FI and BI cameras is seen. For the FI CCD a strong absorption in the dead layer structure decreases the QE, while in the case of the BI camera an increase in the efficiency is observed. Secondly, even in an ideal case, due to the absorption in the dead layer structure, the QE of the FI camera would be less than 100%.

In order to derive the experimental QE ratios, the intensities of the measured x-ray characteristic lines were fitted by means of a least-square method employing Voigtian functions. Examples of such fits were already shown in Figs.5–6. Because the experimental setup was identical for both set of measurements, employing the FI camera or the BI one, the ratio of the fitted intensities corresponds to the QE ratio of the two cameras at a given x-ray energy. In the Fig. 17 the measured QE ratio of the FI to the BI CCDs as a function of the photon energy is depicted by blue open circles and the horizontal dashed line corresponds to a QE ratio of one. These

results show that for photon energies above 4.5 keV the FI CCD is more efficient than the BI one and at the highest measured energy the QE ratio is equal to 2.55. In the low energy range the QE of the BI camera is significantly higher. For a photon energy of 1.872 keV just above the Si K edge, corresponding to the Sr $L\beta$ line, the detection efficiency of this camera is higher by a factor of 3.84.

The experimentally derived QE ratios were fitted with a theoretical model based on the analytical formulas (1) and (2). The values of R and CCE were assumed to be the same for both CCDs. Since x-ray radiation is incident on the CCD surface with an angle depending on the measured x-ray energy and the crystal, a correction factor A was added. In fact, this angle of incidence corresponds to the Bragg angle. Therefore, the theoretical formula for the QE ratio can be written as follows:

$$QE(E)_{ratio} = \frac{\left(e^{X_{FI_{SiO_2}} \cdot A(E)} \right) \times \left(1 - e^{X_{FI} \cdot A(E)} \right)}{e^{X_{BI} \cdot A(E)}} \quad (5)$$

$$\text{with } A(E) = \frac{2d \cdot E(\text{keV})}{12.398 \cdot n \cdot L_A(E)}.$$

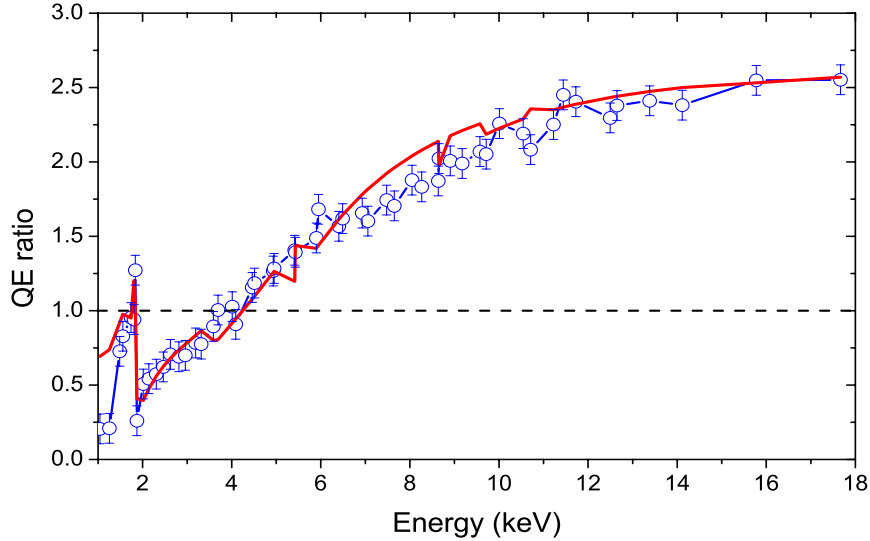


FIG. 17: Measured QE ratios of Front to Back illuminated CCDs as a function of the incoming photon energy (blue open circles). Results of theoretical calculations are also shown (red solid line).

where $X_{FI\text{SiO}_2}$ is the thickness of the dead layer structure in the FI camera and X_{FI} and X_{BI} are the depletion depths for the FI and the BI cameras, respectively. The L_A stands for the absorption length in silicon for a given energy E , whereas n is the reflection order and $2d$ the lattice constants of the crystals given in Table I.

The formula (5) was used to fit the experimental data of the QE ratio. The result is shown as a red solid line in Fig.17. As it can be seen, except below 1.5 keV, the computed curve reproduces well the energy dependency of the measured QE ratios. In particular, the Si K-edge absorption effect at 1.84 keV is well reproduced by the calculations. The small "jumps" observed in the theoretical curve correspond to abrupt changes of the Bragg angle from $\sim 25^\circ$ to $\sim 60^\circ$ when

replacing the crystal of the spectrometer for measuring higher x-ray energies. As a result of the Bragg angle change, the thickness of the CCD chip seen by the photons becomes suddenly smaller than the one corresponding to the measurements performed with the previous crystal, which leads to the observed small dips in the theoretical QE ratio curve.

The best fit of the theoretical function given by the formula (17) to the experimental data was obtained for the following values of the fitting parameters: $X_{FI\text{SiO}_2} = 1 \mu\text{m}$, $X_{FI} = 40 \mu\text{m}$ and $X_{BI} = 15 \mu\text{m}$. The results found for the depletion depths are in good agreement with the values given by the manufacturer (see Table III). For the dead layer thickness of the FI camera, there is no indication in the CCD data sheet but the obtained result agrees reasonably well with

the thicknesses reported for other similar CCD cameras [12, 18].

As the QE ratios of the two cameras can be well reproduced with Eq.(5) derived from the formulas (1) and (2), one could conclude that it should be possible, using the same formulas, to determine the absolute QE of the investigated CCDs. However, to this end the CCE should be known. As this parameter which depends on the photon energy is not provided by the manufacturer, it should be determined experimentally. With the setup employed in the present study, this would represent a difficult task because absolute x-ray intensities are not easy to determine with a crystal spectrometer, some parameters such as the crystal reflectivity being poorly known. Note that because it was assumed that the CCE is the same for both CCDs, this quantity does not appear in the QE ratio formula, but only the well known photon

absorption coefficients.

V. SUMMARY

In conclusion, a variety of characteristic x-ray emission lines were measured with a high-resolution von Hamos curved crystal spectrometer using for the detection of the diffracted x-rays a FI CCD camera and a BI one. From the acquired data the energy response of the two cameras was found to be well linear for both detectors over the energy range between 1 keV and 18 keV. The charge splitting effect was probed as a function of the incoming photon energy and the CCD type. Obtained results could be explained with Monte Carlo simulations. Finally, the QE ratio of the FI to BI camera was determined and compared with theoretical predictions. A good agreement was observed over the whole energy range.

-
- [1] W. Boyle and G. Smith, *Bell Syst. Tech. J.* **49**, 587 (1970).
 - [2] W. Boyle and G. Smith, US patent: 3792322 (1974).
 - [3] J. R. Janesick, *Scientific Charge-Coupled Devices* (SPIE, Washington, 2001).
 - [4] P. Plucinsky et al., *Proc. SPIE* **5488**, 251 (2004).
 - [5] C. D. Mackay, *Ann. Rev. Astron. Astrophys.* **24**, 255 (1986).
 - [6] J. T. Bosiers, I. M. Peters, C. Draijer, and A. Theuwissen, *Nucl. Instrum. Methods Phys. Res.* **A565**, 148 (2006).
 - [7] M. Bregant and E. Milotti, *Nucl. Instrum. Methods Phys. Res.* **A413**, 479 (1998).
 - [8] www.fairchildimaging.com.
 - [9] www.roperscientific.com.
 - [10] www.andor.com.

- [11] www.e2v.com.
- [12] A. Owens, Nucl. Instrum. Methods Phys. Res. **A529**, 391 (2004).
- [13] ST133 Princeton Instruments manual.
- [14] N. Saks, IEEE Elec. Dev. Lett. **EDL-1**, 131 (1980).
- [15] J. Hoszowska et al., Nucl. Instrum. Methods Phys. Res. **A376**, 129 (1996).
- [16] R. D. Deslattes et al., Rev. Mod. Phys. **75**, 35 (2003).
- [17] <http://physics.nist.gov/xcom>.
- [18] M. Pivovarov et al., IEEE Trans. Nucl. Sci. **NS-45**, 164 (1998).
-

Part II

High-resolution study of x-ray resonant Raman scattering at the K-edge of silicon.

J. Szlachetko^{1,3}, J.-Cl. Dousse¹, J. Hozzowska², M. Pajek³, R. Barrett², M. Berset¹,
K. Fennane¹, A. Kubala-Kukus³ and M. Szlachetko¹

¹*Department of Physics, University of Fribourg, CH-1700 Fribourg, Switzerland*

²*European Synchrotron Radiation Facility (ESRF), F-38043 Grenoble, France*

³*Swietokrzyska Academy, Institute of Physics, 25-406 Kielce, Poland*

We report on the first high-resolution measurements of the K x-ray Resonant Raman Scattering (RRS) in Si. The measured x-ray RRS spectra, interpreted using the Kramers-Heisenberg approach, revealed spectral features corresponding to electronic excitations to the conduction and valence bands in silicon. The total cross sections for the x-ray RRS at the $1s$ absorption edge and the $1s-3p$ excitation were derived. The Kramers-Heisenberg formalism was found to reproduce quite well the x-ray RRS spectra, which is of prime importance for applications of the total-reflection x-ray fluorescence technique.

PACS number(s):32.30.Rj, 32.70.Jz, 32.80.Ys, 31.15.Md

The x-ray Raman scattering is a second-order process of photon-atom interaction in which a core-electron is excited into an unoccupied state above the Fermi level by absorption of a photon. This intermediate “virtual” state of the neutral atom decays then radiatively, the initial core hole being filled by another inner-shell electron. The energy of the “scattered” photon $\hbar\omega'$ is given by $\hbar\omega' = \hbar\omega - |B_f| - \epsilon$, where $\hbar\omega$ stand for the energy of the incoming photons, B_f is the binding energy of the inner-shell hole

in the final state, and ϵ is the energy of the excited core-electron above the Fermi level. The cross section for Raman scattering is generally extremely small compared to elastic Rayleigh scattering. However, if the energy of the incoming photon is close to an absorption threshold the Raman process is resonantly enhanced and its cross section increases dramatically. Pioneering works on the x-ray resonant Raman scattering (RRS) using x-ray tubes were performed in the 1970s by Sparks [1] and synchrotron

radiation by Eisenberger et al. [2].

Due to its resonant character, the x-ray RRS is a powerful method to study the electronic structure of solids, being complementary to the x-ray absorption techniques based on the first-order process. High-resolution x-ray RRS measurements represent a novel experimental tool to probe unoccupied states in silicon, giving thus a deeper insight in the electronic structure of this important material for semiconductor industry.

On the other hand, it has been realized that the RRS process sets the limits for application of the total reflection x-ray fluorescence (TXRF) method [3] for measuring very low concentrations of light element impurities on the surface of Si wafers. For instance, several experiments [4, 5] have shown that the detection limit of Al impurities on the Si surface is limited by the presence of RRS x-rays. In fact, for incident photon energies tuned below the Si K -absorption edge to avoid the intense Si K fluorescence x-ray line, the RRS structure of Si is indeed overlapping with the Al K x-ray fluorescence peak. Since the TXRF technique combined with intense synchrotron x-ray sources offers new possibilities for detection of light elements in ultra-clean silicon, a precise knowledge of the x-ray Raman scattering in silicon is therefore crucial for applications of

the TXRF technique in the semiconductor technology. By now, only theoretical predictions [6–10] were available for the RRS structure in silicon. However, to be used for reliable estimations of the detection limits of the TXRF method for light element impurities in silicon, these calculations needed experimental verification.

In this Letter we report on the first high-resolution measurements of the resonant x-ray Raman scattering in silicon, which yielded detailed shapes of the x-ray RRS spectra for TXRF applications. We also demonstrate that both the continuum and bound states close to the threshold can be probed in silicon by means of the RRS technique.

The RRS x-ray spectra were measured at the ESRF beamline ID21 by means of high-resolution x-ray spectroscopy, using a von Hamos Bragg-type curved crystal spectrometer [11] with an energy resolution of about 0.9 eV. The photon beam delivered by the undulator was monochromatized by means of two 20 Å Ni/B₄C multilayers and the residual higher-energy photons were suppressed with a Ni mirror. The monochromator was calibrated by measuring in the fluorescence mode the Al and Si K -absorption edges. Depending on the energy, 10^{12} – 10^{13} incident photons/s with a FWHM energy resolution of ~ 6 eV were obtained

on the sample, which represented a good compromise between an acceptable beam energy resolution and high enough beam intensity to investigate the weak RRS process. For all measurements the angle between the incoming beam and the target surface was set to 20° . Test-measurements performed at smaller incident angles showed too poor RRS yields to be measured in reasonable collecting times by means of high-resolution. A 1 mm thick solid polycrystalline Si sample with a purity better than 99.99% was used.

The measured Si RRS x-ray spectra for beam energies tuned down to -50 eV below the $1s$ absorption edge are shown in Fig.1a, while those measured at energies tuned across the absorption edge, from -6 eV up to $+4$ eV with 2 eV steps, are presented in Fig.1b. As shown, the spectra consist of two components, a broad and asymmetric RRS structure whose position varies with the beam energy and a narrow Si $K\alpha$ fluorescence line which occurs for all beam energies at 1740 eV. The two components are well separated for beam energies smaller by about 10 eV than the Si $1s$ edge (Fig.1a) but are overlapping for energies close to the edge (Fig.1b). The x-ray resonant Raman scattering investigated in the present experiment is due to the excitation of a $1s$ electron into the continuum ($1s-\varepsilon p$) accompanied by a quasi-simultaneous transition of a $2p$

electron to the $1s$ level. The RRS x-ray spectra have very long low-energy tails due to the Lorentzian shapes of the involved atomic levels and sharp high-energy cut-offs. The position of the cut-offs is given by $\hbar\omega' = \hbar\omega - |B_f|$ since $\epsilon = 0$ and is therefore shifted towards higher energies when the beam energy increases. The Si $K\alpha_{1,2}$ fluorescence line ($2p-1s$ transition) results from the photoionization of $1s$ electrons by photons from the high-energy tail of the beam energy distribution. For this reason, the intensity of the Si $K\alpha_{1,2}$ fluorescence line for incident photon energy below the K-edge diminishes rapidly and saturates above the absorption edge.

In order to understand the shapes of the observed spectra, calculations of the x-ray resonant Raman scattering around the K absorption edge were performed within the second-order perturbation theory using the Kramers-Heisenberg formula [7-9]. A more detailed description of these calculations can be found in [10]. The x-ray RRS profiles were computed assuming the excitation of a $1s$ electron into the continuum (above the Fermi level) and a $2p$ vacancy in the final state. The binding energies and natural widths of the $1s$ and $2p$ levels were taken from Refs. [12] and [13], respectively. The oscillator strength distributions $dg_{1s}/d\omega$ (see Ref. [10]) for silicon, needed in the Kramers-

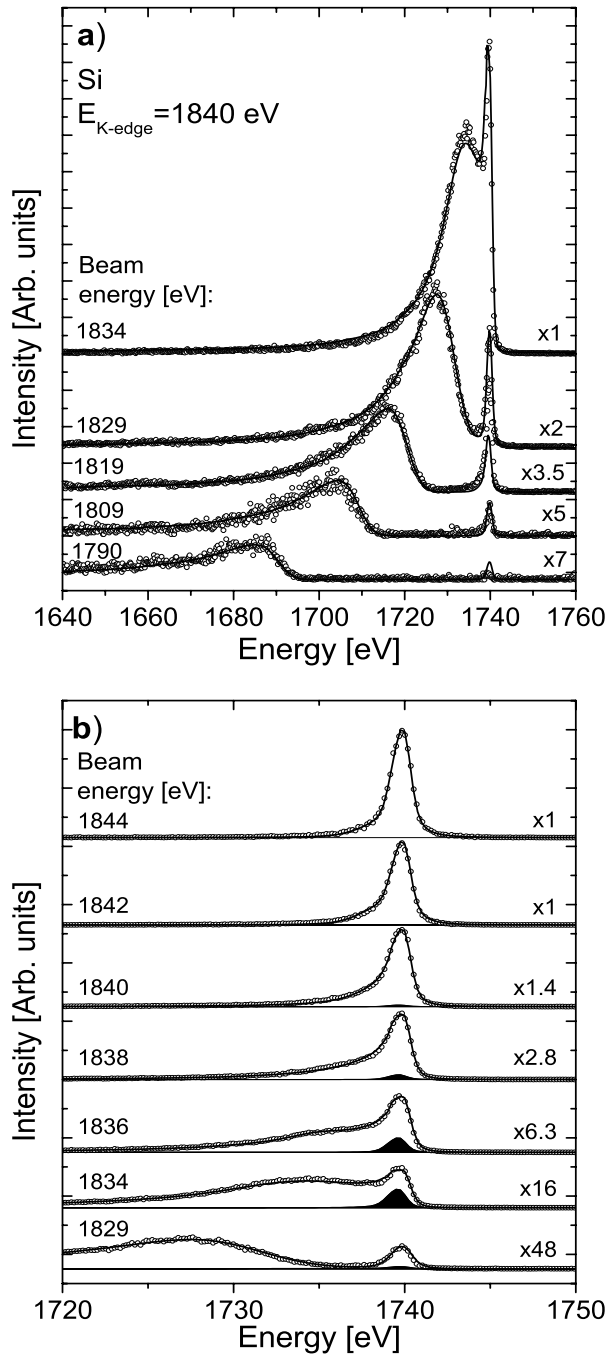


FIG. 1: High-resolution RRS x-ray spectra of Si for incident beam energies tuned a) below the $1s$ absorption edge and b) across it. The open circles represent the measured spectra, the solid black lines the theoretical predictions comprising both the continuum and discrete excitations. The filled areas in b) stand for the predictions corresponding to the discrete excitations. For comparison, the spectra measured at 1829 eV and 1834 eV are presented in a) and b).

Heisenberg approach, were derived from the experimental RRS x-ray spectra in a self-consistent way (see Ref.[14]) by exploiting the fact that the RRS structure measured

for different beam energies is determined by a *common* $dg_{1s}/d\omega$ function. In fact, the oscillator strength distributions extracted from the data for different energies were

found to be very similar, so that the average of these distributions was chosen for $dg_{1s}/d\omega$ in the calculations of the theoretical RRS profiles. The beam energy distribution which was derived from the above mentioned Si K absorption edge measurement, was found to be well reproduced by a Gaussian with a FWHM of 6.1 eV and a small Lorentzian contribution (8%) with a FWHM of 10.0 eV describing the profile tails. To be compared with the experimental RRS spectra, the theoretical profiles were convolved with the beam energy profile and experimental broadening of the spectrometer. The theoretical RRS amplitudes were scaled to match the experimental intensities with the same scaling factor for all spectra. Results of these calculations are presented in Fig.1. As shown, the theoretical shapes are generally in good agreement with the measured ones, demonstrating that the Kramers-Heisenberg approach reproduces fairly well the RRS spectra in a broad range of x-ray energies. In Fig.2, the four most intense x-ray RRS experimental spectra induced by photon beams tuned below the K edge are plotted on the same scale, highlighting the evolution of the RRS spectral features as a function of the beam energy. It can be seen that the low-energy tails of the measured RRS spectra merge together into a single curve. This observation which is expected from

theory is of practical importance for TXRF applications.

A more detailed comparison of the theoretical and experimental spectra showed that for incident energies tuned just below the $1s$ edge the measured intensities slightly below the $K\alpha_{1,2}$ fluorescence line were higher than the calculated ones, when assuming the resonant excitation of $1s$ electrons to the continuum in the RRS process. These discrepancies, peaking at about 1836 eV, suggested the existence of additional, beam energy dependent, $1s-np$ photoexcitations that were not considered in the calculations. Further calculations including the most probable photoexcitation channel for silicon, namely the $1s-3p$, were therefore performed. The generalized Kramers-Heisenberg formula [10] combining both the bound and continuum states was employed. Taking into account that the $3p$ electrons in silicon form the valence band with binding energies in the range from 0 to -5 eV [15] that correspond fairly well to the observed $1s-3p$ excitations centred at about 1836 eV, we found that the present experiment is sensitive enough to observe the $3p$ valence band structure. The measured evolution of the $1s-3p$ excitation as a function of the beam energy is depicted in Fig.1b (filled areas).

In order to suppress the experimental broadening, the oscillator strength distri-

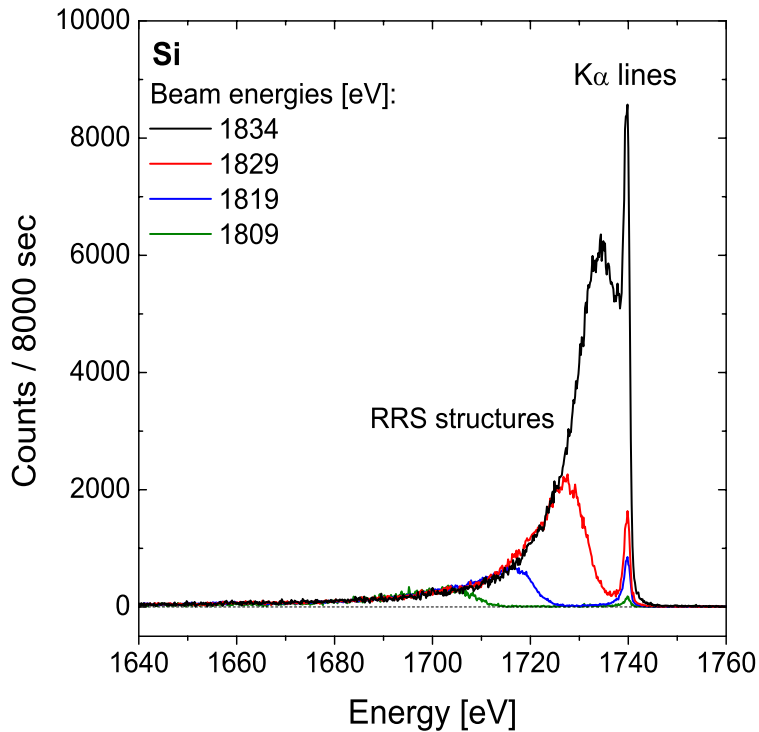


FIG. 2: X-ray RRS spectra measured at different beam energies below the K edge.

bution ($dg_{1s}/d\omega$) obtained from the RRS spectra was further deconvolved for the beam energy profile contribution. Adopting a similar deconvolution procedure as the one proposed by Filliponi [16] for EXAFS applications resulted in an overall resolution of our data of about 3 eV. The deconvolved distribution $dg_{1s}/d\omega$, together with measurements of the linear attenuation coefficients for crystalline and amorphous Si samples taken from [17], is presented in Fig. 3. In fact, both the XANES structure in the near edge region (1840 eV–1855 eV) reflecting the distribution of electronic states in the continuum and the EXAFS oscillations occurring above 1855 eV could be extracted. The

observed differences between the amorphous, polycrystalline and crystalline samples can be attributed to the electron scattering effects reported in [18]. We wish to emphasize, that due to the extremely low cross section of the RRS process, the possibility to obtain EXAFS-like information from RRS measurements for silicon at the K -edge had not been demonstrated experimentally beforehand.

The total cross sections for the RRS process were derived from the experimental intensities of the integrated x-ray RRS spectra normalized to the intensity of the $K\alpha_{1,2}$ x-ray fluorescence line measured at a beam energy of 1895 eV. The K -shell

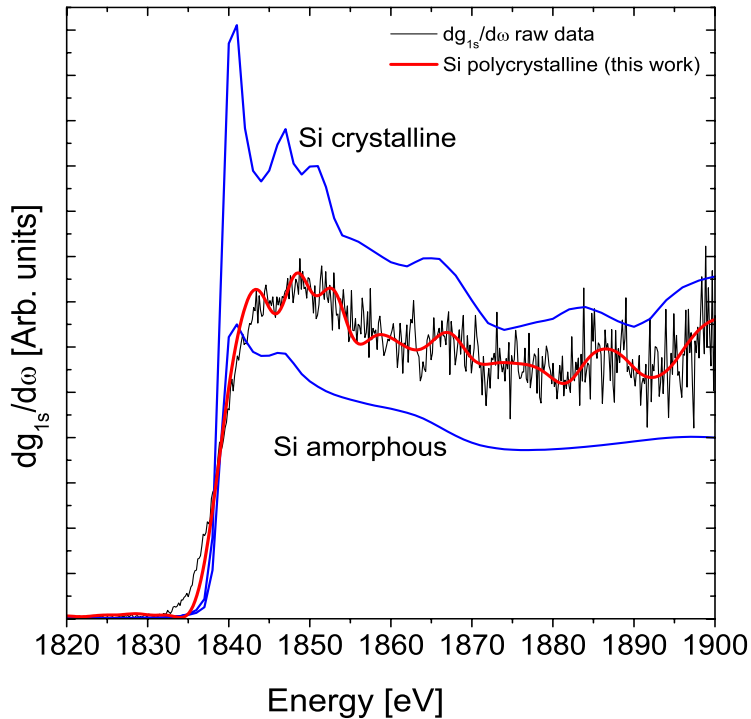


FIG. 3: The oscillator strength distribution $dg_{1s}/d\omega$ obtained from the present RRS measurements for polycrystalline Si compared with the linear attenuation coefficient for amorphous and crystalline Si (from [17]).

photoionization cross section at 1895 eV calculated with the XCOM code [19] was adopted for the normalization and the partial fluorescence yield of the $K\alpha_{1,2}$ transitions was taken from [20]. The same method of normalization was employed to determine the cross section for the $1s-3p$ excitation. All x-ray yields were corrected beforehand for the differences in the self-absorption in the solid Si target of the incident photons and the emitted ones, whereas the crystal reflectivity and CCD efficiency were assumed to be constant over the energy interval covered by our experiment.

The measured total x-ray RRS cross sections are presented as a function of the

incident beam energy in Fig.4. The theoretical RRS cross sections were obtained by integrating the Kramers-Heisenberg formula (see Ref. [10]) over the energy of the emitted photons. As shown, a quite satisfactory agreement is observed. Other experimental data concerning x-ray RRS cross sections, obtained using different techniques, exist only for the photon beam energy of 1740 eV [21, 22]. For the purpose of comparison to these former data, the curve corresponding to the least-squares fit to our results (see Fig.4) was extrapolated to 1740 eV. A value of 5.41 ± 0.61 [barns], i.e. 68.1 ± 7.7 [r_0^2] (where r_0 stands for the classical electron radius) was found, in good agreement with

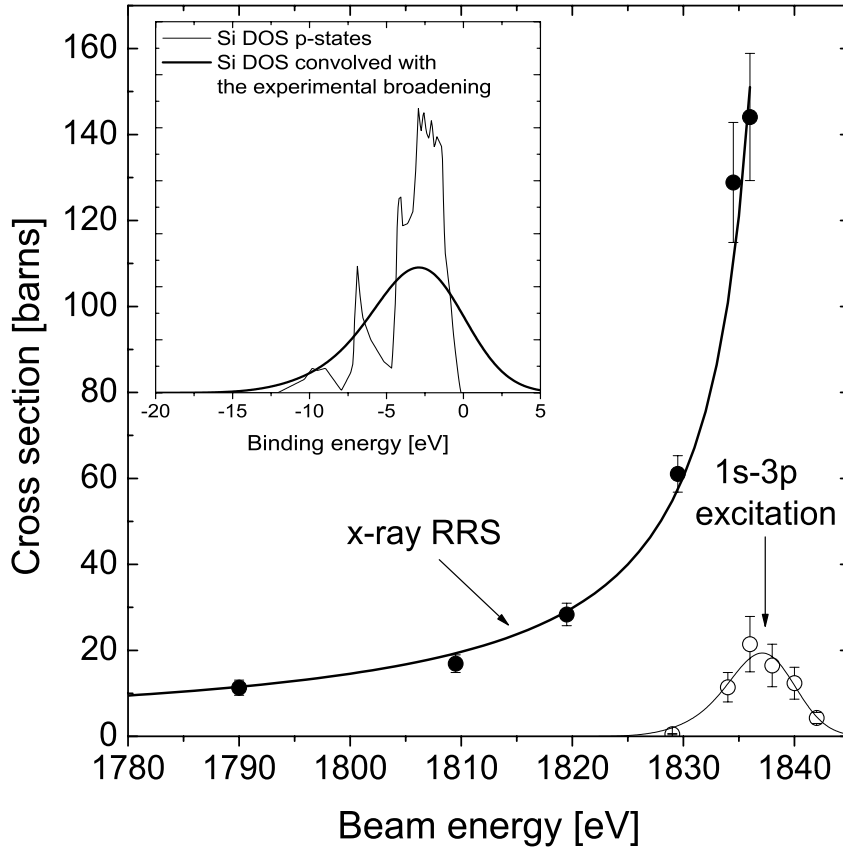


FIG. 4: Measured total cross sections for the Si x-ray RRS (full circles) and $1s-3p$ excitation (open circles) plotted versus the incident photon beam energies. The theoretical RRS predictions are shown by the solid line. Inset shows the density of p states in Si (thin line) convolved with our experimental resolution (thick line). The latter was fitted to the evolution of the observed $1s-3p$ excitation.

the experimental values of $58 \pm 20 [r_0^2]$ and $67 \pm 8 [r_0^2]$ reported in [21] and [22], respectively, and with the theoretical prediction of $61[r_0^2]$ given by Tulkki and Åberg [7].

The x-ray intensities resulting from $1s-3p$ excitation were fitted with a theoretical profile obtained from the density of states (DOS) for Si [15] (inset in Fig.4). The DOS spectrum was convolved with the known experimental broadening and transformed

to a beam energy scale assuming an energy of 1840.1 eV [12] for the $1s$ edge, which corresponds to 0 eV in the DOS curve. Here, we would like to point out that no pre-edge structure was observed by now for Si in near edge x-ray absorption measurements, most probably because of the very small relative intensity (3%) of $1s-3p$ photoexcitation process compared to the x-ray fluorescence.

In conclusion, the x-ray RRS spectra

of Si were measured for the first time by means of high-resolution x-ray spectroscopy. The overall shapes of the observed x-ray RRS spectra were found to be satisfactorily reproduced by calculations based on the Kramers-Heisenberg formalism. The total x-ray RRS cross sections at the Si K -edge were determined and the oscillator strength distribution for continuum states was derived revealing fine details of the electronic structure of silicon. The weak $1s$ - $3p$ photoexcitation was observed in silicon for the first time. Finally, it has to be noted, that the obtained results are of prime importance

for applications of the TXRF technique, which represents the most sensitive method to determine the low-level impurities in Si wafers.

Acknowledgments

The authors would like to thank Dr. R. Tucoulou and his collaborators at the ESRF beam-line ID21 for providing our experiment with very good beam conditions. They also acknowledge the financial support of the Swiss National Science Foundation and the ESRF.

-
- [1] C. J. Sparks, Phys. Rev. Lett. **33**, 262 (1974).
 - [2] P. Eisenberger, P. M. Platzman, and H. Winick, Phys. Rev. Lett. **36**, 623 (1976).
 - [3] R. Klockenkämper, *Total Reflection X-Ray Fluorescence Analysis* (Wiley, New York, 1997).
 - [4] K. Baur et al., J. Appl. Phys. **88**, 4624 (2000).
 - [5] K. Baur et al., Spectrochim. Acta **56B**, 2049 (2001).
 - [6] M. Gavrilă, Rev. Roum. Phys. **19**, 473 (1974).
 - [7] T. Åberg, *Atomic Inner-Shell Physics* (Plenum Press, New York, 1985), pp. 419–463.
 - [8] F. Gel'mukhanov and H. Ågren, Phys. Rep. **312**, 87 (1999).
 - [9] A. Kotani and S. Shin, Rev. Mod. Phys. **73**, 203 (2001).
 - [10] J. Tulkki and T. Åberg, J. Phys. **B15**, L435 (1982).
 - [11] J. Hozzowska et al., Nucl. Instrum. Methods Phys. Res. **A376**, 129 (1996).
 - [12] R. D. Deslattes et al., Rev. Mod. Phys. **75**, 35 (2003).
 - [13] J. L. Campbell and T. Papp., At. Data and Nucl. Data Tables **77**, 1 (2001).
 - [14] H. Hayashi et al., Chem. Phys. Lett. **371**, 125 (2003).
 - [15] P. S. Fowles et al., Phys. Rev. **B48**, 14142 (1993).

- [16] A. Filliponi, J. Phys. **B33**, 2835 (2000).
- [17] A. Owens, G. Fraser, and S. Gurman, Rad. Phys. Chem. **65**, 109 (2002).
- [18] A. Bianconi et al., Phys. Rev. **B36**, 6426 (1987).
- [19] <http://physics.nist.gov/xcom>.
- [20] F. B. Larkins, At. Data Nucl. Data Tables **20**, 313 (1977).
- [21] J. M. Hall et al., Phys. Rev. **A19**, 568 (1979).
- [22] A. G. Karydas, (private communication).
-

High-resolution study of the x-ray resonant Raman scattering process around the 1s absorption edge for aluminium, silicon and their oxides.

J. Szlachetko, J.-Cl. Dousse, M. Berset, K. Fennane, M. Szlachetko
Department of Physics, University of Fribourg, CH-1700 Fribourg, Switzerland

J. Hozzowska, R. Barrett
European Synchrotron Radiation Facility (ESRF), F-38043 Grenoble, France

M. Pajek, A. Kubala-Kukus
Swietokrzyska Academy, Institute of Physics, 25-406 Kielce, Poland

X-ray resonant Raman scattering (RRS) spectra of Al, Al₂O₃, Si and SiO₂ were measured at the European Synchrotron Radiation Facility (ESRF), using a high-resolution Bragg-type curved crystal spectrometer. The x-ray RRS spectra were collected at several beam energies tuned below the 1s absorption thresholds of Al and Si. Differences in the spectral features between the elemental samples and the oxide ones were clearly observed. The data were interpreted using the second-order perturbation theory within the Kramers-Heisenberg (KH) approach. It is shown that, using the KH formalism, oscillator strengths that are similar to the ones deduced from x-ray absorption measurements can be extracted from emission x-ray RRS spectra. The total cross sections for the x-ray RRS process were derived for the different photon beam energies and compared with theoretical predictions. For elemental silicon, the weak 1s-3p excitation was observed for the first time and found to be consistent with results of density of states (DOS) calculations.

PACS number(s): 32.30.Rj, 32.70.Jz, 32.80.Ys, 31.15.Md

I. INTRODUCTION

Intense, monoenergetic and energy-tunable x-ray sources have become a very important tool in material sciences, in particular for the investigation of electronic states and electron-electron correlations

in insulators, semiconductors and metals. Synchrotron radiation has played a major role in this development, being extensively used for state-selective studies in both x-ray absorption spectroscopy (XAS) and x-ray photoelectron spectroscopy (XPS). X-ray

emission spectroscopy (XES) and resonant inelastic x-ray scattering (RIXS) represent alternative techniques to probe electronic excitations in condensed matter systems [1]. However, due to the small signals of XES and RIXS which are spectroscopies of second order optical processes, very intense x-ray sources are needed to obtain precise experimental data. In this respect, a tremendous development of XES and RIXS studies has occurred in the last decade due to the advent of high-brilliance x-ray sources offered by third-generation synchrotron radiation facilities.

Like RIXS, x-ray Raman scattering is a photon-in and photon-out second-order process. In this process a core electron is excited into a bound state just above the Fermi level by absorption of a photon. The intermediate virtual state then decays radiatively, the initial core hole being filled by another inner-shell electron with simultaneous emission of a photon. The energy of the inelastically scattered photon is equal to the energy of the incoming photon minus the sum of the binding energy of the inner-shell hole in the final state and energy above the Fermi level of the excited core electron. In comparison with first-order processes, x-ray Raman scattering intensities are much weaker except if the energy of the incoming photon is close to an absorption threshold. In this case,

the Raman process is resonantly enhanced and its cross section increases drastically. The x-ray resonant Raman scattering (RRS) process can be regarded as a particular case of RIXS in which the scattered photons are characterized by discrete final states [2]. Pioneering works on x-ray RRS were performed in the seventies using x-ray tubes [3] and synchrotron radiation [4].

X-ray RRS has been used extensively in the last years to study the electronic structure of numerous elements and compounds [1]. Up to now, most studies were carried out for transition metals [5–7] and rare earth elements [8, 9] whereas, for low Z elements, x-ray RRS information is more scarce [10–12]. For silicon data were collected mostly about the $L_{2,3}$ edges [13, 14] and more rarely at the K edge [15]. In these experiments, it was shown that the x-ray RRS emission spectra exhibit features which can be used to study the valence and conduction bands. In particular, the shapes of the Si x-ray RRS spectra observed at the L_3 edge were found to be well reproduced by band-structure calculations [16]. In contrast to that, to our knowledge no x-ray RRS study around K -edge has been reported so far for Al, nor for Al_2O_3 . This is somewhat surprising because novel aluminium based materials [17] and aluminium oxides [18], which are widely used in industrial applications have

been intensively investigated using other methods.

The x-ray RRS process also plays an important role in the determination of light element impurities on the surface of ultra clean substrates by means of the total reflection x-ray fluorescence (TXRF) method [19]. The TXRF method is affected by the x-ray RRS process because the latter represents an important source of background. For instance, recent experiments have shown [20, 21] that the detection threshold of Al impurities on the surface of ultra pure silicon wafers is limited by the presence of RRS x-rays. For incident photon energies tuned below the Si $1s$ -absorption edge to avoid the intense Si $K\alpha$ fluorescence peak, the broad x-ray RRS spectrum of Si is indeed overlapping with the Al $K\alpha$ fluorescence line. Detailed knowledge of the shape and yield of the Si x-ray RRS spectrum is therefore crucial for optimisation of the measuring parameters and also assessing the practical minimum detection limits for light element impurities which can be attained. Up to now, due to the lack of existing experimental data, only theoretical predictions [1, 22–24] have been used for the determination of the x-ray RRS background in ultra pure silicon wafers. However, the sensitivity of the TXRF method being limited by the uncertainties related to these calculations, an experimental

verification of the theoretical predictions is highly desirable.

In this paper, we report on high-resolution measurements of the x-ray RRS spectra of Al, Si, Al_2O_3 and SiO_2 . Partial results concerning elemental silicon were already published in [25]. The spectra were collected at several incident photon energies below the K -edges of Al and Si. The shapes of the observed x-ray RRS spectra were compared to predictions based on the Kramers–Heisenberg theory. They were found to be well reproduced by the calculations over wide ranges of beam energy, providing that proper oscillator strength distributions are used. Using the equations proposed by Tulkki and Åberg [22], we were able to extract for all samples the oscillator strength distributions from the corresponding experimental x-ray RRS spectra. The obtained distributions were found to exhibit similar shapes and features as the curves measured by means of the near edge absorption technique. The absolute x-ray RRS cross sections and their variation with the beam energy were determined for the four samples. For elemental silicon, for which data were also taken using beam energies tuned across the K edge, the weak $1s$ – $3p$ excitation could be observed for the first time and its cross section determined.

II. EXPERIMENT

The measurements were performed at the European Synchrotron Radiation Facility (ESRF), in Grenoble, France. The x-ray RRS spectra were measured by means of high-resolution, using a Bragg type von Hamos bent crystal spectrometer [26], installed at the beam line ID21, downstream from the chamber of the scanning transmission x-ray microscope. The spectrometer was equipped with a 10 cm high \times 5 cm wide \times 0.03 cm thick (101) ADP (Ammonium Dihydrogen Phosphate) crystal ($2d=10.642$ Å), curved cylindrically to a radius of 25.4 cm. The x-ray source width, which is crucial for the resolving power of the spectrometer, was defined by a narrow rectangular slit, consisting of two juxtaposed vertical 0.3 mm thick Ta plates, placed between the crystal and the target. By decreasing the slit width the resolution of the spectrometer is improved but its efficiency diminishes. To satisfy at best the conditions of this experiment a slit width of 0.2 mm was chosen. The x-rays diffracted by the crystal were recorded with a position-sensitive back illuminated CCD (Charge Coupled Device) detector consisting of 1340 columns and 400 rows with a pixel size of $20 \times 20 \mu\text{m}^2$. In order to reduce the dark current noise the CCD chip was thermoelectrically cooled down to -50 degrees C. The energy calibration of the

von Hamos spectrometer was determined by measuring the fluorescence $K\alpha$ lines of Al and Si at incident photon energies 50 eV above the K edges of the two elements. These measurements were also used to determine the response function of the spectrometer. The latter was found to be well reproduced by a Gaussian profile with a full width at half maximum (FWHM) of 0.8 eV for Al and 0.9 eV for Si.

The white beam delivered by the ID21 undulator was monochromatized by means of two 20 Å Ni/B₄C multilayers. Higher-energy photons were rejected with an efficiency better than 99.9% by means of a Ni mirror. Depending on the energy, 10^{10} – 10^{11} incident photons per second with a FWHM energy resolution of about 6 eV were obtained on the samples, which represented a good compromise between a high enough beam intensity to observe the weak x-ray RRS spectra and an acceptable beam energy resolution. The monochromator was calibrated in energy by measuring the Al and Si K -absorption edges in the fluorescence mode using a Si(Li) detector.

Solid targets of metallic Al, polycrystalline Si and amorphous Al₂O₃ and SiO₂ with a thickness of 1mm were employed. Purities of the samples were 99.999% for Al and Si, 97.5% for Al₂O₃ and 99.9% for SiO₂. The spot size of the beam on the target was about

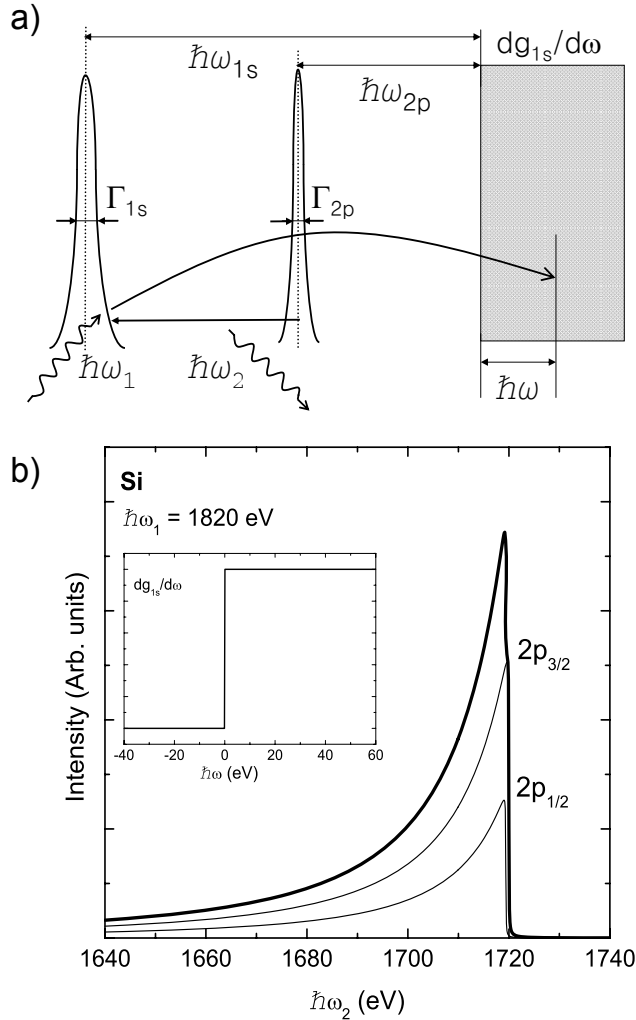


FIG. 1: a) Energy diagram of the x-ray RRS process involving 1s and 2p electrons. b) Theoretical Si x-ray RRS profiles assuming the final vacancy in the L_2 or L_3 subshell (thin solid lines) and their sum (thick solid line). Calculations were done for incoming photons with an energy 20 eV below the K edge. The inset shows the simple step function model used in the calculations for the oscillator strength distribution $dg_{1s}/d\omega$.

1 mm in diameter. For each sample, the angle between the beam and the target surface was set to 20 degrees. Test-measurements performed at smaller incident angles to better reproduce the experimental conditions of low resolution TXRF measurements that are carried out at grazing incidence angles showed x-ray RRS yields too poor to be measured in reasonable collecting times by means of high resolution.

The x-ray RRS data were recorded in the energy range between 1400 eV and 1490 eV

for Al and Al_2O_3 , and between 1640 eV and 1760 eV for Si and SiO_2 . The CCD size along the dispersion axis (26.8 mm) permitted us to cover an energy range of about 40 eV. Thus two to three CCD lengths were required to observe the x-ray RRS spectra of interest. Data were acquired in the so-called multiple frame mode. Numbers of collected images for single measurements varied between 200 and 600 with exposure times of 1s to 10 s per image. Exposure times were chosen depending on the photon intensity on the CCD in order to avoid

multiple hits on single pixels. The CCD camera was operated through a dedicated controller at a rate of 1 MHz so that the time needed to read each two-dimensional image amounted to about 0.5 s. To reject higher order reflection events and diminish the background the acquired images were filtered online by setting suitable energy windows on the CCD. The sum of all filtered images was then projected onto the dispersion axis giving the energy spectrum.

III. THEORY

X-ray RRS differential cross sections can be determined using the formulas developed

by Tulkki and Åberg [22, 23] within the Kramers–Heisenberg model. In the present study the x-ray RRS process consists of the excitation of a $1s$ core electron into an intermediate unoccupied level. This "virtual" state then decays radiatively by a $2p \rightarrow 1s$ transition as schematically shown in Fig.1a. As reported by Åberg and Tulkki [23], the anisotropic interference term between the resonant and nonresonant amplitudes becomes very small close to the K edge. Assuming therefore this term to be negligible in our case, the x-ray RRS differential cross section can be written as follows:

$$\frac{d\sigma(\omega_1)}{d\omega_2} = A \int_0^\infty \frac{\omega_2}{\omega_1} \frac{(\omega_{1s} - \omega_{2p_j})g_{2p_j}(\omega_{1s} + \omega)(dg_{1s}/d\omega)}{(\omega_{1s} + \omega - \omega_1)^2 + \Gamma_{1s}^2/4\hbar^2} \times \frac{\Gamma_{2p_j}/2\hbar}{(\omega_1 - \omega_{2p_j} - \omega - \omega_2)^2 + \Gamma_{2p_j}^2/4\hbar^2} d\omega \quad (1)$$

where A is a normalization constant, $\hbar\omega_1$ and $\hbar\omega_2$ are the energies of the incoming and outgoing photons and $\hbar\omega$ stands for the energy above the Fermi level of the excited electron. The oscillator strength for the $2p \rightarrow 1s$ transition is represented by g_{2p_j} , where $j = 1/2$ or $3/2$, depending on whether the final vacancy is located in the L_2 or L_3 subshell. The $dg_{1s}/d\omega$ represents the oscillator strength dis-

tribution for $1s$ absorption. It is a function of the excited electron energy. The second term in Eq.(1) represents the normalized final state density function that accounts for the final state broadening (Γ_{2p_j}) and ensures the energy conservation which is given by:

$$\hbar\omega_2 = \hbar\omega_1 - \hbar\omega_{2p_j} - \hbar\omega \quad (2)$$

As an example the theoretical x-ray RRS profile given by Eq.(1) is shown in Fig.1b. Calculations were performed for Si assuming an ideally monochromatic beam having an energy of 1820 eV, i.e., an energy 20 eV below the 1s threshold. The binding energies $\hbar\omega_{1s}$ and $\hbar\omega_{2p}$, the atomic level widths Γ_{1s} , Γ_{2p_j} and the oscillator strength g_{2p_j} were taken from [27], [28] and [29], respectively. To simplify the calculations, a step function was assumed for the oscillator strength distribution $dg_{1s}/d\omega$ (see inset in Fig.1b).

As it can be seen from Fig.1b the x-ray RRS profile presents a long low-energy tail which is due to the Lorentzian shape of the involved 1s atomic level. At the low energy limit ($\hbar\omega_2 \rightarrow 0$) the differential cross section $d\sigma(\omega_1)/d\omega_2$ vanishes. The sharp high-energy cut-off is defined by the energy conservation ($\hbar\omega = 0$ in Eq.(2)) and moves towards lower energies when the energy of the incoming photons decreases.

Due to the choice of a step function for the oscillator strength distribution, the theoretical x-ray RRS profile presented in Fig.1b does not show any fine structures. Actually, a more realistic $dg_{1s}/d\omega$ distribution would contain peaks and oscillations similar to those observed in x-ray absorption fine structure (XAFS) spectra. These fine structures should be then reflected in the measured x-ray RRS spectra because in the Raman process by exciting 1s electrons above the Fermi level one scans the density of unoccupied bound states in the atom. As a consequence, realistic $dg_{1s}/d\omega$ distributions should be deducible from experimental x-ray RRS spectra.

In order to calculate analytically the $dg_{1s}/d\omega$, the normalized density function in Eq.(1) can be replaced by the Dirac delta function [23, 30], provided that the width of the final state is negligibly small. Indeed, within this approximation Eq.(1) can be expressed as:

$$\begin{aligned} \frac{d\sigma(\omega_1)}{d\omega_2} &= A \int_0^\infty \frac{\omega_2}{\omega_1} \frac{(\omega_{1s} - \omega_{2p_j})g_{2p_j}(\omega_{1s} + \omega)(dg_{1s}/d\omega)}{(\omega_{1s} + \omega - \omega_1)^2 + \Gamma_{1s}^2/4\hbar^2} \times \delta(\omega_1 - \omega_{2p_j} - \omega - \omega_2)d\omega = \\ &= A \frac{\omega_2}{\omega_1} \frac{(\omega_{1s} - \omega_{2p_j})g_{2p_j}(\omega_{1s} - \omega_{2p_j} + \omega_1 - \omega_2)(dg_{1s}/d\omega)}{(\omega_{1s} - \omega_{2p_j} - \omega_2)^2 + \Gamma_{1s}^2/4\hbar^2} \end{aligned} \quad (3)$$

and the $dg_{1s}/d\omega$ is then given by:

$$\frac{dg_{1s}}{d\omega} = \frac{1}{A} \frac{d\sigma(\omega_1)}{d\omega_2} \frac{\omega_1}{\omega_2} \frac{(\omega_{1s} - \omega_{2p_j} - \omega_2)^2 + \Gamma_{1s}^2/4\hbar^2}{(\omega_{1s} - \omega_{2p_j})g_{2p_j}(\omega_{1s} - \omega_{2p_j} + \omega_1 - \omega_2)}. \quad (4)$$

As the experimental x-ray RRS yield at the energy $\hbar\omega_2$ is proportional to the differential cross section $d\sigma(\omega_1)/d\omega_2$, the latter can be replaced in Eq.(4) by the measured Raman intensity. For a given beam energy ($\hbar\omega_1$) tuned below the $1s$ absorption edge, the profile of the distribution $dg_{1s}/d\omega$ can thus be derived from the corresponding x-ray RRS spectrum for a wide energy range ($\hbar\omega$). Actually, from Eq.(4) two profiles are obtained, that correspond to final vacancy states with $j = 1/2$ and $j = 3/2$, respectively. As only the sum of these two distributions is reflected in the experimental x-ray RRS spectrum, the obtained oscillator strength distribution is a sum of two profiles having similar shapes but shifted in energy. However, for the low- Z samples investigated in the present study, the shifts are only 0.3–0.6 eV [27] and therefore the resulting smearing of the total $dg_{1s}/d\omega$ distributions is small. On the other hand, in contrast to the absorption method, the obtained profile is not broadened by the atomic level width Γ_{1s} of the $1s$ state. Thus, if the experimental broadening is smaller than Γ_{1s} , more detailed $dg_{1s}/d\omega$ profiles can be obtained with this method than with absorption measurements [5].

IV. RESULTS AND DISCUSSION

A. Shape of the RRS x-ray spectra.

The high-resolution x-ray RRS spectra measured for several beam energies tuned below the K absorption edges are depicted in Fig.2 for Al and Al_2O_3 and in Fig.3 for Si and SiO_2 . The energy calibration of the monochromator was obtained by measuring the absorption spectra of the Al and Si samples in the fluorescence mode, assuming for the inflection points the energies of 1559.9 eV and 1840.1 eV reported in [27] for the K edges of these elements. The K edge energies of the two oxides were then deduced from the inflection points of the Al_2O_3 and SiO_2 absorption spectra. Energy shifts of +5.9 eV and +8.0 eV with respect to the parent elements were found for Al_2O_3 and SiO_2 , respectively.

As shown in Figs.2–3 each spectrum consists of two components: a broad structure corresponding to the RRS x-ray spectrum and a narrow line corresponding to the $K\alpha$ x-ray transition. The presence in the observed spectra of the $K\alpha$ x-ray line for beam energies tuned below the $1s$ edge is due to the high-energy tail of the monochromator response. For this reason, the intensity of this line for incident photon energies below the K edge diminishes rapidly and saturates above the absorption edge. The monochromator response was found to be well reproduced by a

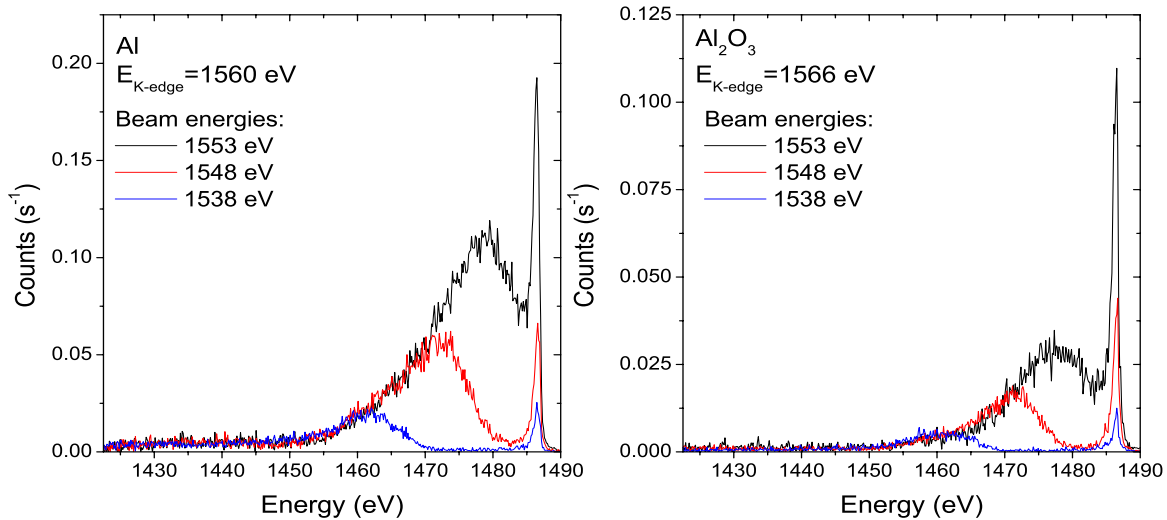


FIG. 2: (Color online) High-resolution x-ray RRS spectra of Al and Al_2O_3 measured for different beam energies tuned below the $1s$ absorption edge.

Gaussian with a FWHM of 6.1 eV and a small Lorentzian contribution (8%) with a FWHM of 10.0 eV accounting for the Lorentzian-like tails characterizing the multilayer monochromator profile.

In general the observed x-ray RRS structures have similar shapes as the ones predicted by theory. In particular, the maxima of the x-ray RRS spectra and the high energy cut-offs move with the beam energy according to the energy conservation law (see Eq.(2)). One can also see that for all samples the tails in the low energy parts of the x-ray RRS structures merge together for any beam energy. This feature of the x-ray RRS spectra may be of practical interest for the TXRF technique. On the other hand, the experimental broadening results in a smearing

of the observed spectra. For this reason, the high energy cut-off as well as the maximum of each RRS structure are significantly wider than those of the theoretical spectrum shown in Fig.1.

B. Oscillator strength distribution

$$dg_{1s}/d\omega$$

In order to extract more detailed information from the observed spectra data were analysed using the Kramers-Heisenberg approach. First of all, a realistic $dg_{1s}/d\omega$ oscillator strength distribution was needed in order to fit properly the RRS spectra. As discussed in sect.III, realistic $dg_{1s}/d\omega$ distributions can be extracted directly from the experimental

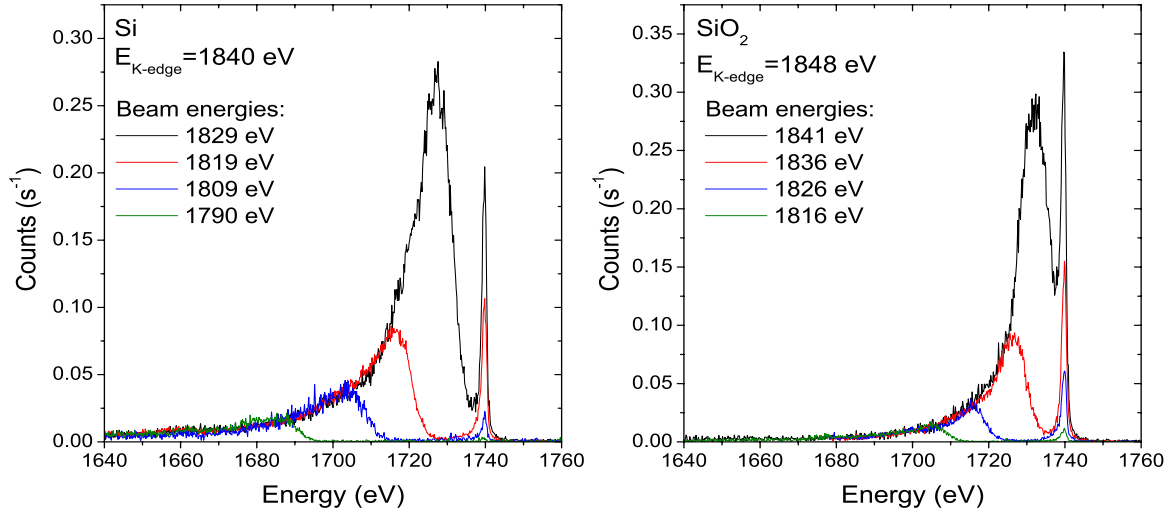


FIG. 3: (Color online) High-resolution x-ray RRS spectra of Si and SiO₂ measured for different beam energies tuned below the 1s absorption edge.

x-ray RRS spectra. The method is explained in more detail below for the case of Si.

At first, the $dg_{1s}/d\omega$ function was determined using Eq.(4). The binding energies were taken from [27], the oscillator strengths g_{2p_j} and the widths of the 1s and 2p states from [29] and [28], respectively. The energy range of the $dg_{1s}/d\omega$ function obtained in this way is limited by the energy domain covered by our measurements. The threshold is given by the cut-off of the emission spectrum and the high-energy limit by the lowest energy of the emitted photons. As a consequence, depending on the beam energy, the extension of the calculated $dg_{1s}/d\omega$ profiles varies. However, in the overlapping region (about 60 eV) the calculated profiles were found to be the same for each beam energy, as expected from

theory, so that the average of these distributions was chosen for $dg_{1s}/d\omega$. For Si, this average distribution is presented in Fig.4 (fluctuating thin solid line). In this figure the energy scale of the excited electrons ($\hbar\omega$) was transformed to the energy scale of the incoming photons ($\hbar\omega_1$) according to Eq.(2), assigning to the origin of the ($\hbar\omega$) scale the energy of 1840.1 eV reported in [27] for the 1s absorption edge. As shown, the obtained distribution has a similar shape as the spectrum measured by the absorption method but, due to the poorer statistics of the x-ray RRS measurements, the $dg_{1s}/d\omega$ distribution is more noisy. In addition, the observed differences in the spectral features at the edge, namely the shift of the first peak and the edge width, are due to the better beam energy resolu-

tion for the absorption spectra measurements. In order to diminish the noise and improve the resolution of the derived distribution, a more sophisticated method of analysis using a dedicated deconvolution procedure was developed.

Among existing spectral deconvolution techniques (see e.g. [31–33]), the method proposed by Filipponi [32] was found to be the most appropriate one to deconvolve XAFS-like functions. Assuming that the measured profile $\frac{\widetilde{dg}_{1s}(E)}{d\omega}$ results from the convolution of the real $dg_{1s}/d\omega$ distribution with the experimental response function G , one can write:

$$\frac{\widetilde{dg}_{1s}(E)}{d\omega} = \int \frac{dg_{1s}(E')}{d\omega} G(E - E') dE' \quad (5)$$

The easiest way to obtain the real function $\frac{dg_{1s}(E)}{d\omega}$ consists to use a deconvolution method based on the Fourier transformation (FT). Within this method, the extracted profile and broadening function are first transformed into the Fourier space, then the first Fourier transform is divided by the second one and the result is finally transformed back into the en-

ergy space:

$$\frac{dg_{1s}(E)}{d\omega} = FT^{-1} \left[FT \left[\frac{\widetilde{dg}_{1s}(E)}{d\omega} \right] / \widetilde{G}(q) \right] \quad (6)$$

where $q = \frac{2\pi}{\hbar\omega}$. In our experiment the broadening was mainly due to the beam energy distribution which could be represented approximately by a Gaussian with a standard deviation σ of about 2.6 eV. In the direct and Fourier spaces the Gaussian broadenings are given respectively by:

$$G(E) = \frac{1}{\sqrt{2\pi}\sigma^2} \exp\left(-\frac{E^2}{2\sigma^2}\right) \quad (7)$$

$$\widetilde{G}(q) = \exp\left(\frac{-\sigma^2 q^2}{2}\right) \quad (8)$$

As in the Fourier transformation the noise blows up even for small values of σ , an additional filter was employed in the deconvolution process. The filter consisted to add a third power term in q in the argument of the $\widetilde{G}(q)$ function to prevent the latter to converge to zero for the $q \rightarrow \infty$ limit. With this filter the deconvolved $dg_{1s}/d\omega$ distribution is finally given by:

$$\frac{dg_{1s}(E)}{d\omega} = FT^{-1} \left[FT \left[\frac{\widetilde{dg}_{1s}(E)}{d\omega} \right] \exp\left(\frac{\sigma^2 q^2}{2} - b(q - q_0)^3\right) \right] \quad (9)$$

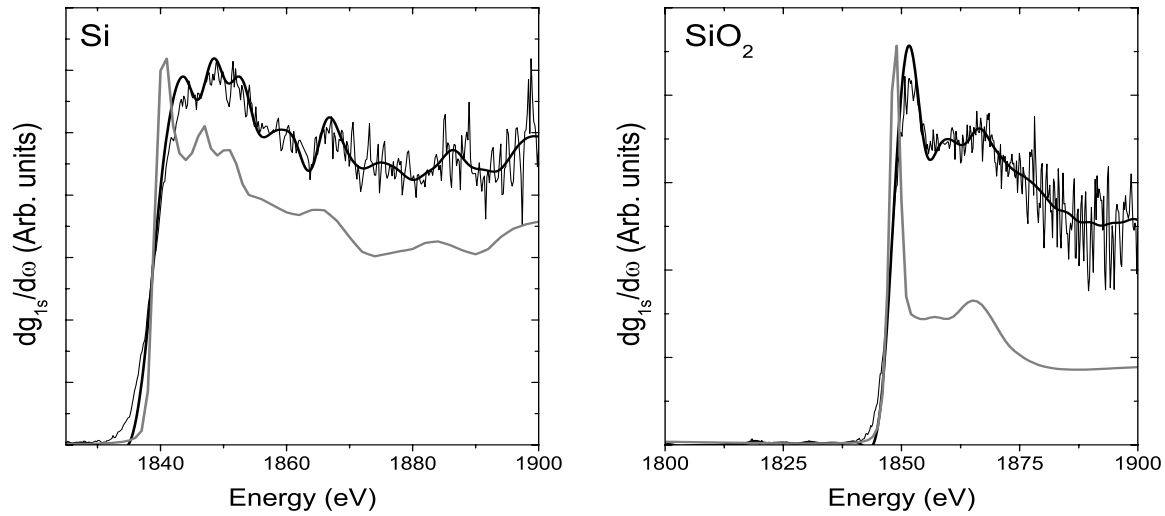


FIG. 4: Oscillator strength distributions obtained for Si and SiO₂ extracted from the corresponding RRS x-ray spectra (thin solid lines). The thick solid lines stand for the distributions that were obtained when a dedicated deconvolution procedure was applied (for details, see text). For comparison the corresponding absorption spectra [34] are also shown (grey lines).

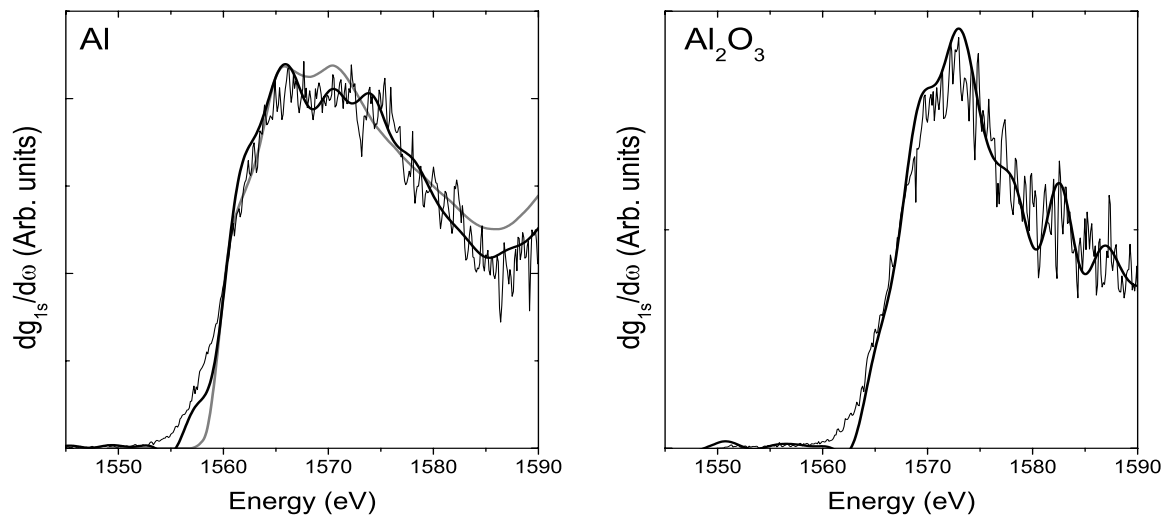


FIG. 5: Oscillator strength distributions obtained for Al and Al₂O₃ extracted from the corresponding RRS x-ray spectra (thin solid lines). The thick solid lines stand for the distributions that were obtained when a dedicated deconvolution procedure was applied (for details, see text). For comparison the absorption spectrum of Al reported in [35] is also shown (grey line).

where b is a constant and q_0 which is of the order of 0.3 eV^{-1} serves to enhance and sharpen the features present in the spectra [32]. When applying the FT a further difficulty resided in oscillations stemming from the step like shape and the finite interval of our distribution. The problem was solved by subtracting a linear function from $\widetilde{dg}_{1s}/d\omega$ so that the first and last points of the distribution had the same value after the subtraction. The linear function was then simply added to the deconvolved distribution since, according to the Cauchy principle, the deconvolution of a linear function results in the same linear function. To check the reliability of the described deconvolution method, the latter was applied to functions resulting from the folding of known profiles. Quite satisfactory results were obtained for the deconvolved curves which were found to match rather well the original ones, neither artificial peaks nor oscillations being observed as a result of the deconvolution.

As the FT is a noise-sensitive process, raw data were smoothed before their deconvolution, using the Slavitzky-Golay filter. As it can be seen from Fig.4, the noise level is not constant but grows with energy. Actually this is not surprising because the high-energy part of the $dg_{1s}/d\omega$ distribution corresponds to the low-energy part of the emission spectrum where the fluctuations are much bigger

than in the near cut-off region. For this reason, before smoothing the data, a variable binning was employed in which the number of binned points was increased with energy, in order to bring the normalized sums of binned points to the same statistical error. However, to preserve the fine structures present in the spectrum, the energy range corresponding to the binned points was always kept smaller than the experimental resolution.

The result of the deconvolution of the previously smoothed $\widetilde{dg}_{1s}/d\omega$ distribution of Si is depicted in Fig.4 (thick solid line). As shown a significant improvement is brought by the binning-smoothing procedure. For instance, the small structures around 1870 eV and 1885 eV are better resolved and in the near edge region a triplet structure appears which was hardly visible before.

The same deconvolution method was employed for SiO_2 , Al and Al_2O_3 . Results are presented in Fig.4 and Fig.5, respectively. At first one sees that significant differences are observed between Al and Si, although the two elements differ only by one unit in the atomic number Z , as well as between the pure elements and their oxides. A further inspection of the two figures shows that for Si, SiO_2 and Al the overall shapes of the derived distributions are similar to those obtained by means of absorption measurements. For Al_2O_3 , no comparison could be performed

since no corresponding XANES (near edge x-ray absorption spectroscopy) spectrum for an amorphous sample was found.

In the case of Si, the triplet structure appearing around 1842 eV reflects the density of states of the conduction band [36] while the structures at 1862 eV and 1883 eV are due to the multiple scattering effects reported in [37]. A similar triplet structure is observed in the near edge region of SiO₂ in good accordance with the absorption spectra reported in [34, 36, 38]. The strong white line around 1850 eV, which is less sharp and shifted to higher energies in our case as a result of the poorer beam energy resolution, has been assigned in [36] to an excitonic state with p symmetry. Regarding Al, the near edge structure can be interpreted in terms of unoccupied levels with a majority contribution of p and d states as discussed in [35].

Here, we would like to point out that the possibility to obtain XAFS-like information over a wide energy range from x-ray RRS spectra has not been demonstrated experimentally beforehand, probably because of the extremely low x-ray RRS cross sections. In fact, as shown in the present paper, x-ray RRS measurements can represent an alternative to absorption measurements for studying the electronic properties in materials.

C. Shape of the x-ray RRS spectra vs. Kramers–Heisenberg formalism

The $dg_{1s}/d\omega$ distributions derived with the method described in the preceding section can now be employed to calculate the shapes of the x-ray RRS spectra using the Kramers–Heisenberg formula. An example of the results obtained from these numerical calculations is shown for SiO₂ in Fig.6.

The energies of the $1s$ and $2p$ levels of SiO₂, which are needed in the calculations, were derived directly from the experiment. At first, the energy of the $1s$ level was determined from the inflection point of the K -absorption edge measurement. A value of 1848.1 eV was found. The energies of the two $2p$ levels were then determined by subtracting from the above value the fitted energies of the $K\alpha_{1,2}$ doublet measured in the off-resonance regime. Results of 108.1 eV and 107.5 eV were obtained for the $2p_{1/2}$ and $2p_{3/2}$ levels, respectively. The fitted Lorentzian widths of the $K\alpha_1$ and $K\alpha_2$ lines were found to be the same as those obtained in the fit of elemental Si, so that the widths Γ_{1s} and Γ_{2p} and the oscillator strength g_{2p_j} occurring also in the Kramers–Heisenberg formula were assumed to be the same as those reported for Si in [28, 29].

The x-ray RRS profile calculated by means of Eq.(1) as well as the fluorescence

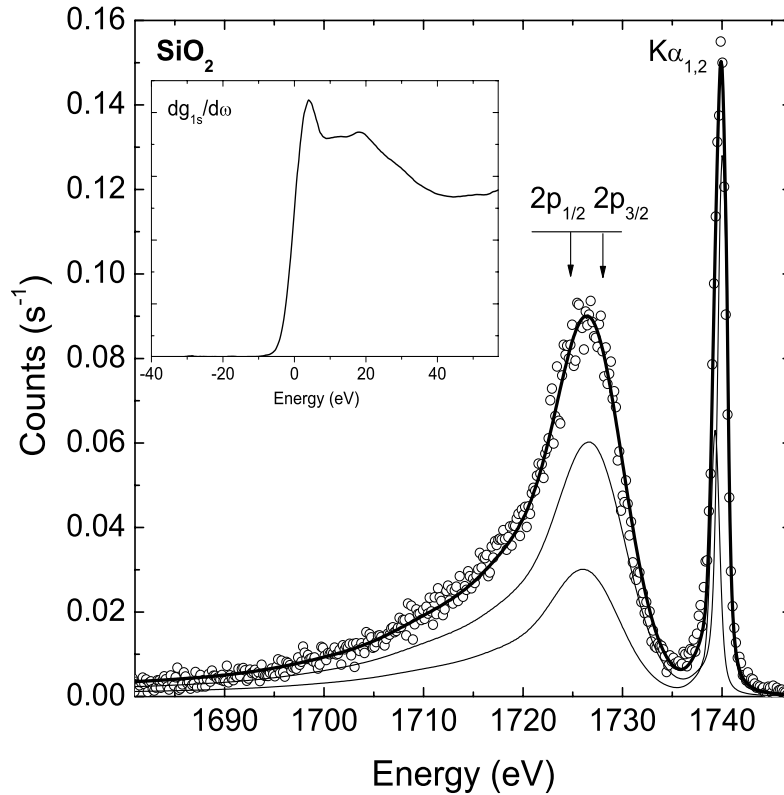


FIG. 6: Theoretical shape of the x-ray RRS spectrum of SiO_2 calculated for an excitation energy of 1836 eV (thick solid line). Thin lines correspond to final states with the vacancy in the L_2 and L_3 subshells. The open circles represent the experimental spectrum. The oscillator strength distribution used in the calculations is shown in the inset.

$K\alpha$ line were then fitted to the data. As shown in Fig.6 a quite satisfactory agreement was achieved. Similar good agreements between the shapes of the experimental and theoretically computed spectra were observed for the other samples and any employed beam energy. Note that for a given sample the theoretical x-ray RRS yield was scaled to match the experimental intensity but the same scaling factor was then used for the x-ray RRS spectra taken at different energies. It can be concluded that the shapes of

x-ray RRS spectra can be well reproduced by the Kramers–Heisenberg approach, using the Tulkki and Åberg formula. However, we have found that good fits to the experimental data were only obtained when the proper $dg_{1s}/d\omega$ distribution was used in the calculations. This is probably not true for low-resolution ($\Gamma_{exp} > 100$ eV) TXRF measurements, for which precise enough theoretical x-ray RRS spectra can be computed using a simple step function for the $dg_{1s}/d\omega$ distribution.

D. X-ray RRS cross sections

The total cross sections for the x-ray RRS process were derived from the experimental intensities of the integrated x-ray RRS spectra normalized to the intensity of the parent $K\alpha$ x-ray lines measured at beam energies about 50 eV above the $1s$ thresholds. Assuming that the x-ray RRS cross section for photon energies slightly below the K -edge is isotropic [23], the following relation was employed:

$$\sigma_{RRS} = \frac{I_{RRS}}{I_{K\alpha}} \sigma_K \omega_{K\alpha} \quad (10)$$

where I_{RRS} and $I_{K\alpha}$ correspond to the integrated yields of the x-ray RRS spectra and $K\alpha$ transitions. The single K shell photoionization cross sections σ_K and the partial fluorescence yields $\omega_{K\alpha}$ were taken from [39] and [40], respectively. All x-ray yields were corrected for the differences in the absorption in the target of the incoming and outgoing photons, whereas the efficiency of the crystal spectrometer was assumed to be constant over the about 100 eV wide energy intervals covered by the present experiment.

The energy range of the x-rays emitted in the RRS process extends down to 0 eV, whereas only photons with energies bigger than the lower limits (E_{min}) of the measured energy intervals were observed. The value of E_{min} was 1400 eV for Al and Al_2O_3 and 1640

eV for Si and SiO_2 . The problem was solved by extending the calculations of the theoretical x-ray RRS profiles down to 0 eV and by integrating then the theoretical spectra from zero to E_{min} . The so-obtained theoretical yields were then simply added to the measured x-ray RRS intensities to get the total x-ray RRS yields employed in the cross section determination. Since the shapes of the experimental x-ray RRS spectra were found to be very well reproduced by theory over the whole photon energy intervals covered by the measurements, one can expect that the corrections for the missing experimental x-ray RRS yields obtained this way are reliable. Furthermore, as the low energy tails of the x-ray RRS spectra merge together below the maxima of the spectra (see Fig.2 and Fig.3), for a given sample the correction should be the same for any beam energy. This was confirmed by the calculations within the statistical uncertainties so that the same average yield correction was applied to all x-ray RRS spectra corresponding to the same target.

The total x-ray RRS cross sections obtained in the present work are presented in Fig.7 for the four samples. The cross sections corresponding to the missing experimental x-ray RRS yields discussed above amount to 0.166 cm^2/g and 0.125 cm^2/g for Al and Al_2O_3 , respectively to 0.123 cm^2/g and 0.072 cm^2/g for Si and SiO_2 . The solid lines in Fig.7

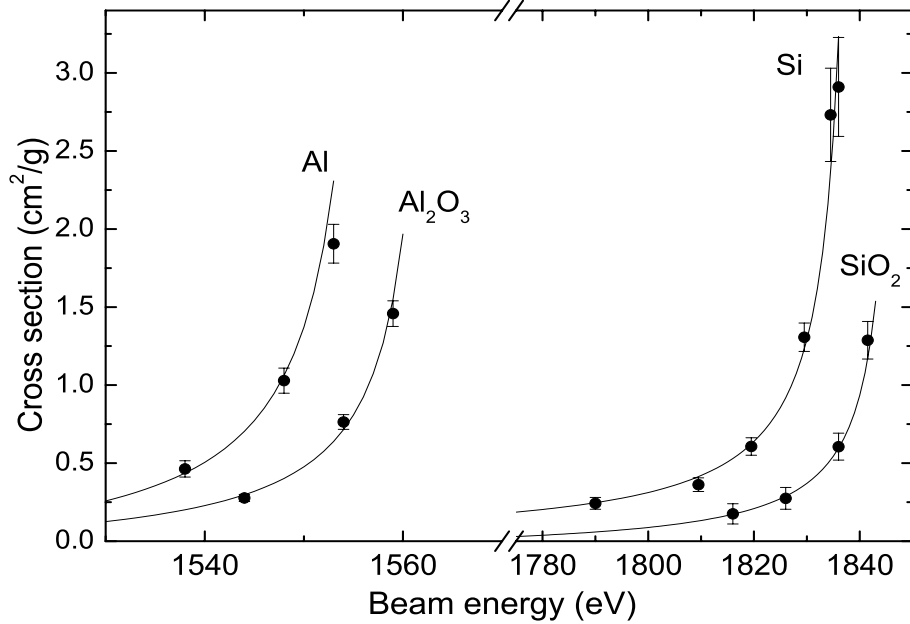


FIG. 7: Total x-ray RRS cross sections plotted versus the photon beam energies. The solid lines represent the corresponding theoretical cross sections computed by means of the Kramers–Heisenberg formula.

correspond to theoretical predictions based on the Kramers–Heisenberg formula. They were calculated by integrating Eq.(1) over the whole energy range of the emitted photons, i.e. from $\hbar\omega_2 = 0$ to $\hbar\omega_2 = E_{cut-off}$. The constants A occurring in Eq.(1) were determined by fitting the theoretical cross section curves to the experimental points. As showed by the figure the beam energy dependency of the theoretical cross sections is in good agreement with the experimental data.

Because the $1s$ absorption edges lie 6 eV (Al_2O_3), respectively 8 eV (SiO_2), higher than those of the corresponding pure elements, the cross section curves of the ox-

ides are shifted towards higher beam energies. Furthermore, a careful inspection of Fig.7 shows that for the same energy differences with respect to the K edges, the x-ray RRS cross sections of the compounds are smaller by about a factor 2. This is due to the fact that the cross sections presented in the figure are expressed in cm^2/g and the number of Al or Si atoms per mass unit is about 2 times smaller in the oxides than in the pure elements (1.88 times smaller for Al_2O_3 and 2.14 for SiO_2). Converting in barns per atom the cross sections obtained for instance at beam energies 10 eV below the K -edges, one finds values of 61.8 b/atom and 75.5 b/atom

for Al and Al₂O₃, and of 60.5 b/atom and 71.5 b/atom for Si and SiO₂. Approximately the same ratios $(RRS)_{oxide}/(RRS)_{element} \cong 1.2$ are obtained for other excitation energies. It seems therefore that the x-ray RRS cross sections of Al and Si are about 20% bigger in the oxides than in the pure elements when expressed in barns per atom. This is, however, not really unexpected, the unoccupied states above the Fermi level involved in the x-ray RRS process being affected by the chemical environment.

Other experimental data concerning x-ray RRS cross sections are very scarce and exist only for elemental Si [41–43]. Available data were determined by means of different techniques employing low-resolution detectors. Results reported in [41] and [42] were obtained using the $K\alpha$ x-rays of Si as incoming photons (1740 eV). Cross sections of 58 ± 20 [r_0^2] [41] and 67 ± 8 [r_0^2] [42] (where r_0 stands for the classical electron radius) were found. To compare our Si results to these former data, the curve corresponding to the least-squares fit to present Si cross sections was extrapolated to 1740 eV. A value of 0.116 ± 0.013 cm²/g, i.e., 68.1 ± 7.7 [r_0^2] was obtained in good agreement with the above-mentioned experimental results and with the theoretical value of 61 [r_0^2] reported by Åberg and Tulkki [23].

Very recently, a new set of experimental

Si x-ray RRS differential cross sections was published [43]. The cross sections were determined for a wide energy range of incident photons (1580 eV–1822 eV). The Si target was irradiated with monochromatized synchrotron radiation (resolving power of about 1000) and the scattered radiation was measured with a Si(Li) detector. From the curve reported in Fig.6 of this paper, differential cross sections of 5.1 ± 0.4 [$r_0^2 \text{sr}^{-1}$], 14.4 ± 1.0 [$r_0^2 \text{sr}^{-1}$] and 46.9 ± 3.3 [$r_0^2 \text{sr}^{-1}$] corresponding to beam energies of 1740 eV, 1800 eV and 1825 eV were deduced. Using the values of the least squares fit to our results corresponding to the three energies and transforming them into the same units, differential cross sections of 5.4 ± 0.6 [$r_0^2 \text{sr}^{-1}$], 14.5 ± 1.4 [$r_0^2 \text{sr}^{-1}$] and 41.6 ± 3.7 [$r_0^2 \text{sr}^{-1}$] are found that are again consistent within the combined errors with the ones from [43]. However, for beam energies close to the 1s edge (e.g., the third chosen energy in the above comparison), the results reported in [43] seem to be somewhat bigger than ours. A plausible explanation for the deviations, if any, may reside in some contamination of the x-ray RRS spectra of [43] by the fluorescence $K\alpha$ line of Si. At beam energies close to the 1s threshold, the $K\alpha$ line can indeed be induced by photons from the high-energy tail of the beam energy distribution, leading to some excess of intensity in the x-ray RRS spectra since $K\alpha$ x-rays cannot be

separated from high-energy x-ray RRS photons in low-resolution measurements.

E. Measurements across the $1s$ absorption edge for Al and Si.

For Al and Si, the measurements were extended to beam energies tuned across the K edge. The corresponding x-ray RRS spectra

are presented in Fig.8 and Fig.9. From the two figures, the evolution of the target x-ray emission from the fluorescence $K\alpha$ emission to the x-ray RRS emission while the beam energy is tuned across the edge is clearly visible. As also shown by the figures, the overall x-ray emission yields diminish drastically with the beam energy as soon as the latter is

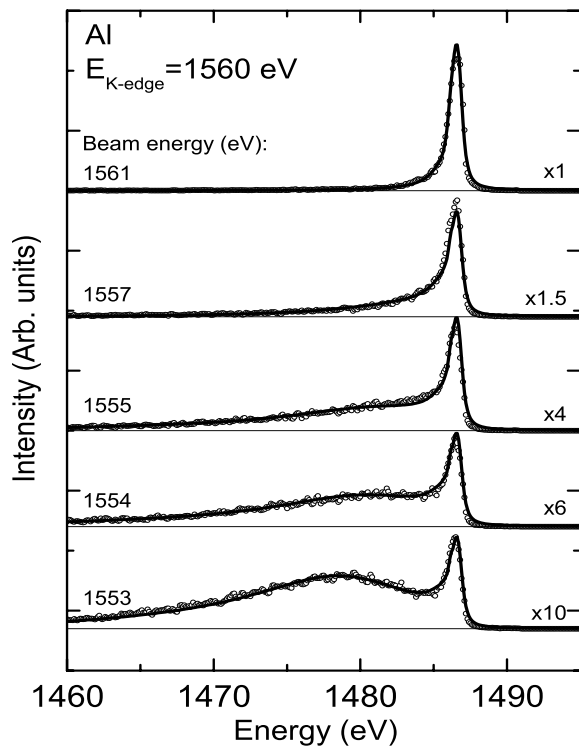


FIG. 8: High-resolution RRS x-ray spectra of Al for incident beam energies tuned across the $1s$ absorption edge. The open circles represent the experimental spectra, the solid lines the theoretical predictions calculated with the Kramers-Heisenberg formula for continuum excitations. For comparison with the yields of the x-ray RRS spectra depicted in Fig.2 the spectrum measured at 1553 eV is shown again.

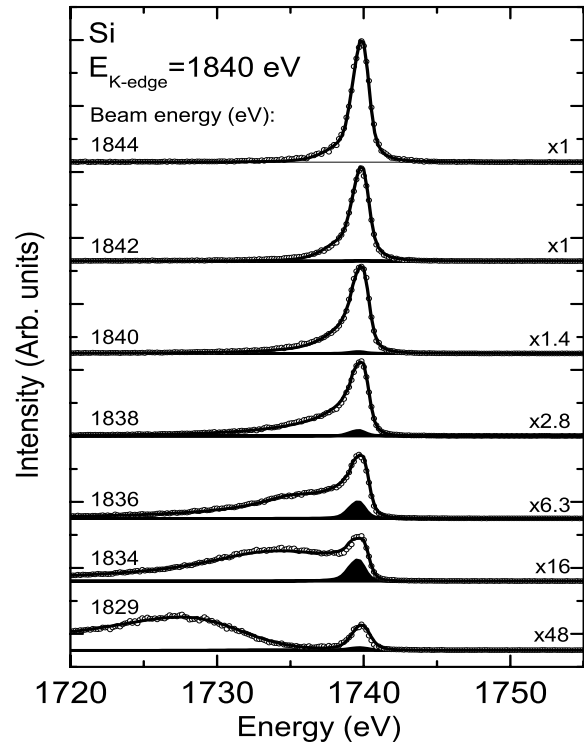


FIG. 9: High-resolution RRS x-ray spectra of Si for incident beam energies tuned across the $1s$ absorption edge. The open circles represent the experimental spectra, the solid lines the theoretical predictions comprising both the continuum and discrete excitations and the filled areas the discrete $1s-3p$ excitation. For comparison with the yields of the x-ray RRS spectra depicted in Fig.3 the spectrum measured at 1829 eV is shown again.

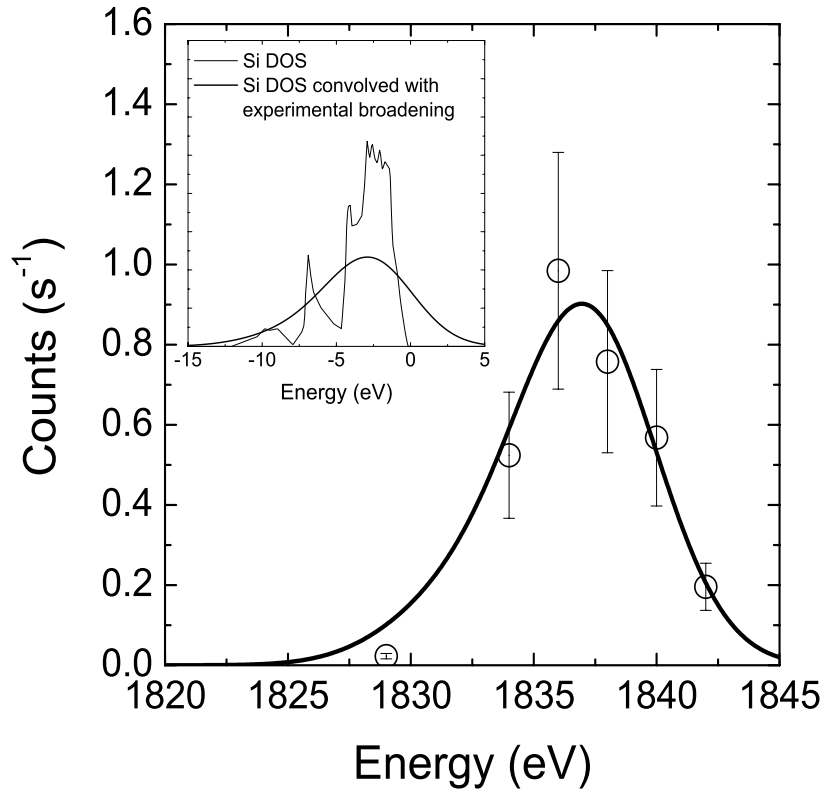


FIG. 10: Measured intensity evolution of the Si $1s$ - $3p$ excitation (open circles). The thick solid line represents the fit to the data of the convolved DOS function. The DOS profile of the Si $3p$ states is depicted in the inset (thin solid line) as well as the convolution of this profile with the experimental response function (thick solid line).

tuned below the $1s$ edges.

Measurements in the near edge region are interesting because they permit to probe the goodness of calculations in the energy region corresponding to the $\hbar\omega_1 \rightarrow \hbar\omega_{1s}$ limit, where there is a transition from the x-ray RRS process towards characteristic fluorescence. On the other hand, when the beam energy is tuned close to the absorption threshold one can hope to observe excitations to discrete unoccupied levels. From the experimental point of view, however, measurements across the $1s$ edge are difficult because the absorption of the beam in the target varies rapidly.

Very careful beam energy dependent corrections for the intensity attenuation of the incoming photons in the target were necessary to obtain reliable results. This point was crucial for the present experiment since thick targets were employed.

To reproduce the evolving shape of the x-ray emission spectra observed in the near edge region, each spectrum was considered as the sum of a x-ray RRS profile and a $2p$ - $1s$ transition. The x-ray RRS profiles of the two samples were determined by means of the Tullki and Åberg formula using the oscillator strength distributions determined from

the spectra measured below the edges (see sect.IV B). For each sample, all x-ray RRS profiles were normalized in intensity with the same scaling constant. The shapes and positions of the Al and Si $K\alpha$ lines were kept constant in the calculations, using the centroid energies and widths obtained from the fits of the lines measured 50 eV above the edges. The variation of the intensity of the $K\alpha$ line across the edge was computed using the intensity measured above the edge and correcting it by the relative number of incident photons having an energy bigger than the $1s$ threshold. As for each measurement the position and shape of the beam energy profile (area normalized to 1) were known, the fraction of incoming photons having enough energy to produce a $1s$ photoionization was determined by integrating the beam profile, using as lower integration limit the $1s$ threshold energy.

Results of these calculations are shown in

Figs.8 and 9 (thick solid lines). From Fig.8 one sees that for aluminium the experimental spectra are well reproduced by the calculations. In the case of silicon, some discrepancies between theory and experiment were observed for beam energies tuned slightly below the $1s$ absorption edge, the calculated intensities of the $K\alpha$ line being systematically lower than the measured ones. These deviations which were found to vary with the beam energy, the maximum being observed at 1836 eV, suggested the existence of additional, beam energy dependent, $1s$ - np photoexcitations that were not considered in the calculations. Further calculations were thus performed, using the generalized Kramers-Heisenberg formalism which allows the inclusion of discrete excitations, by assuming $dg_{1s}/d\omega = g_{1snp} \cdot \delta(\omega_{np} + \omega)$ in Eq.(1) [23]. Within this formalism, the line shape of the $1s$ - np photoexcitation can be described by the following equation [22, 23]:

$$\frac{d\sigma_{np}(\omega_1)}{d\omega_2} = A \frac{\omega_2 (\omega_{1s} - \omega_{2p_j}) g_{2p_j} (\omega_{1s} - \omega_{np}) g_{1snp}}{\omega_1 (\omega_{1s} - \omega_{np} - \omega_1)^2 + \Gamma_{1s}^2/4\hbar^2} \frac{\Gamma_{2p_j}/2\hbar}{(\omega_1 - \omega_{2p_j} + \omega_{np} - \omega_2)^2 + \Gamma_{2p_j}^2/4\hbar^2} \quad (11)$$

The most probable $1s$ - np photoexcitation in silicon corresponds to $n=3$. The $3p$ levels are valence band states with binding energies between 0 and 5 eV. This energy interval is

consistent with the energy difference between the $1s$ threshold (1840 eV) and the energy for which the biggest intensity deviation was observed (1836 eV). Actually, assuming

that the intensity deviations between theory and experiment are due to the $1s-3p$ excitation, the variation of the deviations as a function of the beam energy corresponds to the evolution with energy of the $1s-3p$ photoexcitation. This evolution is depicted in Fig.10 (open circles). In the inset of Fig.10 results of density of states (DOS) calculations for the $3p$ states of Si taken from [44] are presented (thin solid line). Convoluting the DOS distribution with the known experimental broadening results in the curve represented in the inset by the thick solid line. The convolved curve was then fitted to the observed intensity deviations, using the curve centroid position and the area as free fitting parameters. The best fit result is represented by the thick solid line in Fig.10. The weighted average position given by the fit is 1836.4 eV. Since the K -edge energy of Si was determined to be 1840.1 eV, an average binding energy of -3.7 eV is found for the $3p$ level, in fair agreement with the weighted average value deduced from the DOS calculations (-3.5 eV).

A third term corresponding to the $1s-3p$ excitation was thus added in the computation of the theoretical shapes of the Si spectra measured across the K -edge. As shown in Fig.9, in which the $1s-3p$ excitation contributions are represented by filled areas, the experimental spectra are well

reproduced by the calculations for all beam energies, included those around 1836 eV where significant deviations were observed before considering the $1s-3p$ excitation. At this point, we would like to point out that the $1s-3p$ photoexcitation in Si has not been observed before, neither in XANES spectra nor in XES measurements. This is most likely due to the weakness of the cross section for the $1s-3p$ excitation. The latter could be determined from our measurements. A value of 19.6 ± 6.3 barns/atom was found for incident photons of 1836.9 eV, a value which is about 7000 times weaker than the $1s$ photoionization cross section. For Al the $1s-3p$ excitation was not observed. This is, however, not unexpected since in metals the valence and conduction bands overlap, and because a high photon beam energy resolution is required to probe discrete excitations to unfilled upper levels.

V. SUMMARY

In conclusion, the x-ray RRS spectra of Al, Al_2O_3 , Si and SiO_2 were measured by means of high-resolution x-ray spectroscopy using monochromatized synchrotron radiation whose energy was tuned below and across the K absorption edges of Al and Si. The observed shapes of the x-ray RRS

spectra could be well reproduced by calculations based on the Kramers–Heisenberg formalism, but only when realistic oscillator strength distributions were employed in the calculations. As predicted by theory the observed x-ray RRS spectra are characterized by high energy cut-offs and long low-energy tails. These tails merge together in the low energy range, no matter which beam energy is used. For all samples, the oscillator strength distributions could be extracted from the measurements. They were found to exhibit structures similar to those observed in absorption measurements. The total cross sections for the x-ray RRS process were determined as a function of the beam energy. The variation of the cross sections with the beam energy could be well reproduced by theory. For Si, the cross sections were compared to the few existing experimental and theoretical data. A quite

satisfactory agreement was observed. Tuning the beam energy across the $1s$ absorption edge of silicon, we were able to observe the discrete $1s$ – $3p$ excitation for the first time. The evolution of the excitation cross section with the beam energy was found to well reproduce the probability density of unoccupied $3p$ states predicted by DOS calculations.

Acknowledgments

The authors would like to thank Dr. R. Tucoulou and his collaborators at the ESRF beam line ID21 for providing our experiment with very good beam conditions. They are also grateful to Dr. A. Mihelic from I.J.S., Ljubljana, for helpful discussions about the deconvolution problematics. The financial support of the Swiss National Science Foundation and the ESRF is acknowledged.

-
- [1] A. Kotani and S. Shin, Rev. Mod. Phys. **73**, 203 (2001).
 - [2] A. Simionovici, J. P. Briand, P. Indelicato, and P. Chevallier, Phys. Rev. **A41**, 3707 (1990).
 - [3] C. Sparks, Phys. Rev. Lett. **33**, 262 (1974).
 - [4] P. Eisenberger, P. Platzman, and H. Winick, Phys. Rev. Lett. **36**, 623 (1976).
 - [5] H. Hayashi et al., Phys. Rev. **B68**, 045122 (2003).
 - [6] M. Magnuson et al., Phys. Rev. **B68**, 045119 (2003).
 - [7] G. Ghiringhelli et al., Phys. Rev. Lett. **92**, 117406 (2004).
 - [8] S. M. Butorin et al., Phys. Rev. Lett. **77**, 574 (1996).
 - [9] H. Hayashi et al., Phys. Rev. **B70**, 155113 (2004).

- [10] J. A. Carlisle et al., Phys. Rev. Lett. **74**, 1234 (1995).
- [11] J. A. Carlisle et al., Phys. Rev. **B59**, 7433 (1999).
- [12] A. Kikas et al., Phys. Rev. **B70**, 085102 (2004).
- [13] J.-E. Rubensson et al., Phys. Rev. Lett. **64**, 1047 (1990).
- [14] S. Shin et al., Phys. Rev. **B53**, 15660 (1996).
- [15] Y. Ma et al., Phys. Rev. Lett. **74**, 478 (1995).
- [16] S. Eisebitt et al., J. Electr. Spectr. Relat. Phenom. **93**, 245 (1998).
- [17] D. Aswal et al., J. Appl. Phys. **98**, 026103 (2005).
- [18] R. French, J. Am. Ceram. Soc. **73**, 447 (1990).
- [19] R. Klockenkamper, *Total Reflection X-Ray Fluorescence Analysis* (Wiley, New York, 1997).
- [20] K. Baur, J. Kerner, S. Brennan, A. Singh, and P. Pianetta, J. Appl. Phys. **88**, 4624 (2000).
- [21] K. Baur, S. Brennan, B. Burrow, D. Werho, and P. Pianetta, Spectrochim. Acta **56B**, 2049 (2001).
- [22] J. Tulkki and T. Åberg, J. Phys. **B15**, L435 (1982).
- [23] T. Åberg and J. Tulkki, *Atomic Inner-Shell Physics* (Plenum Press, New York, 1985), pp. 419–463.
- [24] F. Gel'mukhanov and H. Ågren, Phys. Rev. **A49**, 4378 (1994).
- [25] J. Szlachetko et al., Phys. Rev. Lett. **97**, 073001 (2006).
- [26] J. Hoszowska et al., Nucl. Instrum. Methods Phys. Res. **A376**, 129 (1996).
- [27] R. D. Deslattes et al., Rev. Mod. Phys. **75**, 35 (2003).
- [28] J. L. Campbell and T. Papp, At. Data and Nucl. Data Tables **77**, 1 (2001).
- [29] J. H. Scofield, Phys. Rev. **A9**, 1041 (1974).
- [30] H. Hayashi, Y. Udagawa, W. A. Caliebe, and C.-C. Kao, Phys. Rev. **B66**, 033105 (2002).
- [31] P. K. Gupta, J. Phys. **D3**, 1919 (1970).
- [32] A. Filipponi, J. Phys. **B33**, 2835 (2000).
- [33] G. M. Petrov, J. Quant. Spec. Radiat. Transf. **72**, 281 (2002).
- [34] A. Owens, G. W. Fraser, and S. J. Gurman, Rad. Phys. Chem. **65**, 109 (2002).
- [35] E. Tamura, J. van Ek, M. Froba, and J. Wong, Phys. Rev. Lett. **74**, 4899 (1995).
- [36] N. Nagashima et al., Phys. Rev. **B48**, 18257 (1993).
- [37] A. Bianconi et al., Phys. Rev. **B36**, 6426 (1987).
- [38] Y. Baba, T. A. Sasaki, and H. Yamamoto, Phys. Rev. **B49**, 709 (1994).
- [39] <http://physics.nist.gov/xcom>.
- [40] F. B. Larkins, At. Data Nucl. Data Tables **20**, 313 (1977).

- [41] J. M. Hall et al., Phys. Rev. **A19**, 568 (1979).
- [42] A. G. Karydas, (private communication).
- [43] M. Müller, B. Beckhoff, G. Ulm, and B. Kanngiesser, Phys. Rev. **A74**, 012702 (2006).
- [44] P. S. Fowles et al., Phys. Rev. **B48**, 14142 (1993).

List of publications

Referred articles

Chemical effects in the $K\beta$ x-ray emission spectra of sulfur.

M. Kavcic, J.-Cl. Dousse, J. Szlachetko, W. Cao.

Nuclear Instruments and Methods B, accepted for publication.

High-resolution study of x-ray resonant Raman scattering process around 1s absorption edge for aluminium, silicon, and their oxides.

J. Szlachetko, J.-Cl. Dousse, J. Hozzowska, M. Pajek, R. Barrett, M. Berset, K. Fennane, A. Kubala-Kukus, M. Szlachetko.

Physical Review A75, 022512 (2007).

A 2D position sensitive germanium detector for spectroscopy and polarimetry of high-energetic x-rays.

Th. Stohlker, U. Spillmann, D. Banas, H.F Beyer, J. Cl. Dousse, S. Chatterjee, S. Hess, C. Kozhuharov, M. Kavcic, T. Krings, D. Protic, R. Reuschl, J. Szlachetko, S. Tachenov, S. Trotsenko.

Journal of Physics: Conference Series 58, 411 (2007).

High-resolution study of x-ray resonant Raman scattering at the K-edge of silicon.

J. Szlachetko, J.-Cl. Dousse, J. Hozzowska, M. Pajek, R. Barrett, M. Berset, K. Fennane, A. Kubala-Kukus, M. Szlachetko.

Physical Review Letters 97, 073001 (2006).

State-selective x-ray study of the radiative recombination of U^{92+} ions with cooling electron.

M. Pajek, Th. Stohlker, D. Banas, H. F. Beyer, S. Boehm, F. Bosch, C. Brandau, M. Czarnota, S. Chatterjee, J.-C. Dousse, A. Gumberidze, S. Hagmann, C. Kozhuharov, D. Liesen, P. H. Mokler, A. Müller, R. Reuschl, E. W. Schmidt, D. Sierpowski, U. Spillmann, J. Szlachetko, S. Tachenov, S. Trotsenko, P. Verma, M. Walek, A. Warczak and A. Wilk.

Photonic, Electronic and Atomic Collisions, Proceedings of the 14th ICPEAC conference, 289, (2006).

Resonant x-ray Raman scattering for Al, Si and their oxides.

J. Szlachetko, R. Barrett, M. Berset, J.-Cl. Dousse, K. Fennane, J. Hoszowska, A. Kubala-Kukus, M. Pajek, M. Szlachetko.

Nuclear Instruments and Methods in Physics Research B 238, 353-356 (2005).

Conference abstracts***Investigation of Depth Profiles in Trace Elements Distributions in Wooden Sculptures with XRF Method.***

J. Braziewicz, R. Dudzik, A. Kubala-Kukus, M. Paciorek, M. Pajek, J. Rutkowski, M. Stankiewicz, J. Szlachetko, J. Semaniak.

17th International Congress on X-ray Optics and Microanalysis, Chamonix 2003, France.

Resonant Raman scattering for Al, Si and their oxides.

J. Szlachetko, R. Barrett, M. Berset, J.-Cl. Dousse, K. Fennane, J. Hoszowska, A. Kubala-Kukus, M. Pajek, M. Szlachetko.

4th Conference on Synchrotron Radiation in Materials Science, Grenoble 2004, France.

X-ray resonant Raman scattering in Si at 1s absorption edge.

J. Szlachetko, R. Barrett, M. Berset, J.-Cl. Dousse, K. Fennane, J. Hoszowska, A. Kubala-Kukus, M. Pajek, M. Szlachetko.

ESRF Users Meeting, Grenoble 2005, France.

Size-dependent $K\beta$ resonant X-ray emission spectra of MnO_2 nanopowder.

J. Hoszowska, M. Berset, J.-Cl. Dousse, K. Fennane, J. Szlachetko, M. Szlachetko.

ESRF Users Meeting, Grenoble 2005, France.

First high-resolution study of the double 1s photoionization of Mg.

J.-Cl. Dousse, J. Hoszowska, M. Berset, K. Fennane, J. Szlachetko, M. Szlachetko.

20th International Conference on X-ray and Inner-Shell Processes, Melbourne 2005, Australia.

Size-dependent resonant K x-ray emission spectra of Mn and Fe oxide nanopowders.

J. Hoszowska, M. Berset, J.-Cl. Dousse, K. Fennane, J. Szlachetko, M. Szlachetko.

20th International Conference on X-ray and Inner-Shell Processes, Melbourne 2005, Australia.

X-ray resonant Raman scattering in Si and SiO_2 at Si-K absorption edge.

J. Szlachetko, R. Barrett, M. Berset, J.-Cl. Dousse, K. Fennane, J. Hoszowska, A. Kubala-Kukus, M. Pajek, M. Szlachetko.

XXIV International Conference on Photonic, Electronic and Atomic Collisions, Rosario 2005, Argentina.

First high-resolution observation of X-ray resonant Raman scattering in Si at 1s absorption edge.

J. Szlachetko, R. Barrett, M. Berset, J.-Cl. Dousse, K. Fennane, J. Hoszowska, A. Kubala-Kukus, M. Pajek, M. Szlachetko.

International Workshop on Photoionization, Campinas 2005, Brazil.

High-resolution study of the x-ray resonant Raman scattering for Al, Si, Al₂O₃ and SiO₂ in the region of the K-absorption edge.

M. Szlachetko, R. Barrett, M. Berset, J.-Cl. Dousse, K. Fennane, J. Hoszowska, A. Kubala-Kukus, M. Pajek, J. Szlachetko.

International Workshop on Photoionization, Campinas 2005, Brazil.

High resolution study of the resonant Raman scattering in the region of Xe L₃ edge.

M. Zytник, M. Kavcic, K. Bucar, A. Mihelic, J. Koktajl, J. Szlachetko.

2nd International Conference on Current Developments in Atomic, Molecular and Optical Physics with Applications, New Delhi 2006, India.

X-ray resonant Raman scattering in Si and SiO₂ at Si K-absorption edge.

A. Kubala-Kukus, J. Szlachetko, R. Barrett, M. Berset, J.-Cl. Dousse, K. Fennane, J. Hoszowska, M. Pajek, M. Szlachetko.

8th International School and Symposium on Synchrotron Radiation in Natural Sciences, Zakopane 2006, Poland.

X-ray resonant Raman scattering below the Si-K absorption edge.

M. Pajek, J. Szlachetko, A. Kubala-Kukus, R. Barrett, M. Berset, J.-Cl. Dousse, K. Fennane, J. Hoszowska, M. Pajek, M. Szlachetko.

European Conference on X-Ray Spectrometry, Paris 2006, France.

Chemical effects in the K x-ray emission spectra in sulfur.

M. Kavcic, J.-Cl. Dousse, J. Szlachetko, W. Cao.

European Conference on X-Ray Spectrometry, Paris 2006, France.

Double photoionization of Ca and V beyond maximum.

J. Hoszowska, J.-Cl. Dousse, K. Fennane, W. Cao, M. Kavcic, J. Szlachetko, M. Szlachetko.

European Conference on X-Ray Spectrometry, Paris 2006, France.

Double K-shell ionization of magnesium and aluminium.

J.-Cl. Dousse, J. Hoszowska, K. Fennane, W. Cao, M. Kavcic, J. Szlachetko, M. Szlachetko.

European Conference on X-Ray Spectrometry, Paris 2006, France.

Performance Test of a 2D -Strip Ge(i) Detector.

Th. Stohlker, U. Spillmann, D. Banas, H.F. Beyer, J. Cl. Dousse, S. Chatterjee, S. Hess, C. Kozhuharov, M. Kavcic, T. Krings, D. Protic, R. Reuschl, J. Szlachetko, S. Tachenov, S. Trotsenko.

Nuclear Science Symposium, Medical Imaging Conference and 15th International Room Temperature Semiconductor Detector Workshop, San Diego 2006, USA.

Relative detection efficiency of back- and front-illuminated CCD cameras for x-rays between 1keV and 18 keV.

J. Szlachetko, J.-Cl. Dousse, J. Hoszowska, M. Kavcic, W. Cao, M. Szlachetko.
ESRF Users Meeting, Grenoble 2007, France.

Non-refereed publications and scientific reports

High-resolution measurements of x-ray RRS of Si and Al and their oxides.

J. Szlachetko, R. Barrett, M. Berset, J.-Cl. Dousse, K. Fennane, J. Hoszowska, A. Kubala-Kukus, M. Pajek, M. Szlachetko.
ESRF Scientific Report 2004.

State-selective x-ray study of the radiative recombination of U92+ ions with cooling electron.

M. Pajek, Th. Stlker, D. Banas, M. Czarnota, J.-C. Dousse, A. Gumberidze, R. Reuschl, E. W. Schmidt, D. Sierpowski, U. Spillmann, J. Szlachetko, S. Tachenov, S. Trotsenko, P. Verma, M. Walek, A. Warczak.
Annual Report 2004, Swietokrzyska Akademy.

Resonant Raman scattering for Al, Si and their oxides.

J. Szlachetko, R. Barrett, M. Berset, J.-Cl. Dousse, K. Fennane, J. Hoszowska, A. Kubala-Kukus, M. Pajek, M. Szlachetko.
Annual Report 2004, Swietokrzyska Akademy.

Double K-shell photoionization of Mg, Al and Si from threshold to saturation.

J. Hoszowska, M. Berset, J.-Cl. Dousse, K. Fennane, J. Szlachetko, M. Szlachetko.
ESRF Scientific Report 2005.

Performance test of a 2D μ -strip Ge(i) detector at the synchrotron facility ESRF.

Th. Stlker, U. Spillmann, D. Banas, H.F. Beyer, J. Cl. Dousse, S. Chatterjee, S. Hess, C. Kozhuharov, M. Kavcic, T. Krings, D. Protic, R. Reuschl, J. Szlachetko, S. Tachenov, S. Trotsenko.
GSI Scientific Report 2005.

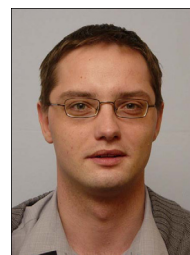
X-ray study of the enhancement effect in radiative recombination of bare U⁹²⁺ ions with low-energy electrons.

M. Pajek, Th. Stlker, D. Banas, H. F. Beyer, S. Boehm, F. Bosch, C. Brandau, M. Czarnota, S. Chatterjee, J.-C. Dousse, A. Gumberidze, S. Hagmann, C. Kozhuharov, D. Liesen, P. H. Mokler, A. Mller, R. Reuschl, E. W. Schmidt, D. Sierpowski, U. Spillmann, J. Szlachetko, S. Tachenov, S. Trotsenko, P. Verma, M. Walek, A. Warczak and A. Wilk.
GSI Scientific Report 2005.

Curriculum vitae

Personal information

First name: Jakub
Last name: Szlachetko
Date of Birth: 10 June 1977
Place of Birth: Kielce, Poland
Nationality: Polish
Marital status: married



Education

07.2003–06.2007

Physics Department, University of Fribourg, Switzerland

Ph.D. student and assistant in the Atomic Physics Group (Prof. Dr. Jean-Claude Dousse)

Title of the Ph.D. thesis: "X-ray resonant Raman scattering in light elements and Relative detection efficiency of Charge Coupled Devices"

10.1998–06.2003

Institute of Physics, Holy Cross Academy, Kielce, Poland

Master student in the Atomic Physics Group (Prof. Dr. Marek Pajek)

Title of the Master thesis: "Trace element contamination control by means of the total reflection x-ray spectroscopy"

09.1994 – 06.1998

Secondary school, Kielce, Poland

09.1986 - 06.1994

Primary school, Kielce, Poland

Diplomas

Master of Physics (Holy Cross Academy, Kielce, Poland)

Secondary school Certificate

Acknowledgments

*A journey is easier
when you travel together.*

This Ph. D. thesis is a result of four years of work. During this time, many people have given me their support and guidance. It is a pleasure to have the opportunity to express my gratitude to all of them.

First of all, I would like to thank Prof. Jean-Claude Dousse who has guided my research work with enthusiasm and constant help. His integral view on research, experience and passion for physics were for me a source of great motivation. Being always a patient supervisor, he has steered my work caring for its high-quality in every respect. I was lucky to have a chance to work with such an excellent physicist.

I would also like to deeply thank Prof. Marek Pajek for all the ideas and criticism. His comments and suggestions always served as a source of never-ending discussions. Thanks to his constant encouragement, I was able to achieve more and more ambitious goals. I owe him a lot.

I thank Dr. Joanna Hoszowska for all her help. Her invaluable experience in synchrotron radiation helped me a lot in learning and understanding experimental physics.

I also thank all colleagues and friends who had worked with me during my study: Michel Berset, Matjaz Kavcic, Yves Kayser, Wei Cao, Karima Fennane and Yves-Patrik Maillard. Special thanks go to my friends from Kielce: Aldona Kubala-Kukus and Darek Banas.

I am also grateful to the administrative and workshop staff of the Physics Department for their kindness and help.

Last but most important, I wish to thank my wife Monika who had patiently tolerated my working weekends. It is impossible to express how much her everyday support has helped me in completing my Ph. D. study.

Szczególnie chce podziękować całej mojej rodzinie za wsparcie i pomoc podczas moich studiów w Szwajcarii. Dziękuje rodzicom, którzy zawsze we mnie wierzyli.